

# **Understanding the nanoscale structure of hexagonal phase lyotropic liquid crystal membranes**

Benjamin J. Coscia,<sup>†</sup> Richard D. Noble,<sup>†</sup> Douglas L. Gin,<sup>†,‡</sup> Joe Yelk,<sup>¶</sup> Matthew A. Glaser,<sup>¶</sup> Xunda Feng,<sup>§</sup> and Michael R. Shirts<sup>\*,†</sup>

<sup>†</sup>*Department of Chemical and Biological Engineering, University of Colorado Boulder,  
Boulder, CO 80309, USA*

<sup>‡</sup>*Department of Chemistry and Biochemistry, University of Colorado Boulder, Boulder CO  
80309, USA*

<sup>¶</sup>*Department of Physics, University of Colorado Boulder, Boulder CO, 80309, USA*

<sup>§</sup>*Department of Chemical and Environmental Engineering, Yale University, New Haven,  
Connecticut 06511, USA*

E-mail: michael.shirts@colorado.edu

## Abstract

Nanostructured porous membranes made from the cross-linked hexagonal phase of self-assembled lyotropic liquid crystals (LLCs) are a promising material for selective separations. In this work, we develop an atomistic molecular model of an LLC membrane. We show that our model is maximally consistent with experimental observations by comparing simulated X-ray Diffraction (XRD) patterns and calculated ionic conductivity to their experimental counterparts. We explore, in depth, the composition and structure of the nanopores in order to give insights that are not easily accessible to experimentalists. The clearer picture of the nanoscopic structure of these membranes provided in this study will enable a better understanding of the mechanisms of small molecule transport within these nanopores.

## Introduction

Figure S 2

A highly selective membrane would be useful for the recovery of valuable products from complex aqueous and organic solutions. For example, flowback water (FW) produced during hydraulic fracturing is a complex wastewater full of potentially valuable dissolved organic compounds such as acetate.<sup>1</sup> There is increasing pressure to reuse hydraulic fracturing water rather than dispose of it in order to reduce social and environmental impacts as well as cost.<sup>2</sup> Rather than dispose of the wastestream generated in the recycling process, we can instead use highly selective membranes in order to successfully recover useful compounds.

Selective separation by a semipermeable membrane barrier is a function of the geometric and chemical interactions of solutes with the membrane material. A molecule's size, shape, charge and polarity combine to determine the degree to which a solute partitions into a membrane and how fast it travels through the membrane. To separate a component from a mixture, one must understand how to design membranes in order to tune the relative transport rates of desired and undesired solutes.<sup>3,4</sup>

Crosslinked lyotropic liquid crystal (LLC) membranes may be capable of performing highly selective separations. LLCs are amphiphilic molecules that have the ability to self-assemble into porous nanostructures<sup>5</sup> which can be crosslinked to create mechanically strong membrane films with pores on the order of 1 nm in diameter.<sup>6</sup> Unlike commercial NF membranes, LLC membrane pores are uniform in size. Since LLC membranes lack a pore size distribution, they inherently exhibit high selectivity due to their strict molecular weight cut-off (MWCO).<sup>6</sup> Additionally, the LLC monomers described in this paper are salts, and therefore lead to Donnan exclusion of ions in solution. The membrane gains a net surface charge when counterions from head groups that line the pore walls escape into the feed solution in order to balance the gradients of concentration and electric potential.<sup>7</sup>

The feasibility of LLC membranes has been demonstrated using LLCs that form the type I bicontinuous cubic ( $Q_I$ ),<sup>8–10</sup> and the inverted hexagonal ( $H_{II}$ )<sup>6</sup> phases (See Figure 1). When separating organic solutes from NaCl,  $Q_I$  phase membrane filtration experiments have shown selectivity 2–3 times higher than commercial RO and 6–12 times higher than commercial NF membranes.<sup>1</sup> When separating a series of various sized dyes, the  $H_{II}$  phase membrane showed complete rejection of dyes bigger than 1.2 nm in size.<sup>6</sup>

The  $H_{II}$  phase pore geometry is has a higher theoretical capacity for transport than the  $Q_I$  phase. The  $H_{II}$  phase forms at room temperature in the presence of c.a. 10 wt% water and consists of hexagonally packed, hydrophilic pore columns.<sup>5</sup> In the absence of water, neat monomer will form the same hexagonal columnar structure which, in literature, has been referred to as the  $Col_h$  thermotropic phase<sup>11</sup> (See Figure 1b). The most promising  $Q_I$  phase for membrane applications forms at 70°C when monomer is mixed with c.a. 20 wt% glycerol.<sup>10</sup>  $Q_I$  phase membranes consist of a tortuous network of three dimensionally interconnected pores that prevent optimal through-plane transport. The densely packed, non-tortuous and uniform sized pores of  $H_{II}$  phase membranes represents the ideal geometry for achieving high solute flux.<sup>12</sup> Despite the promise of the  $H_{II}$  phase, the hexagonally packed liquid crystalline domains, formed during self-assembly of NA-GA3C11 monomers, are isotropically aligned

which is detrimental to membrane performance.

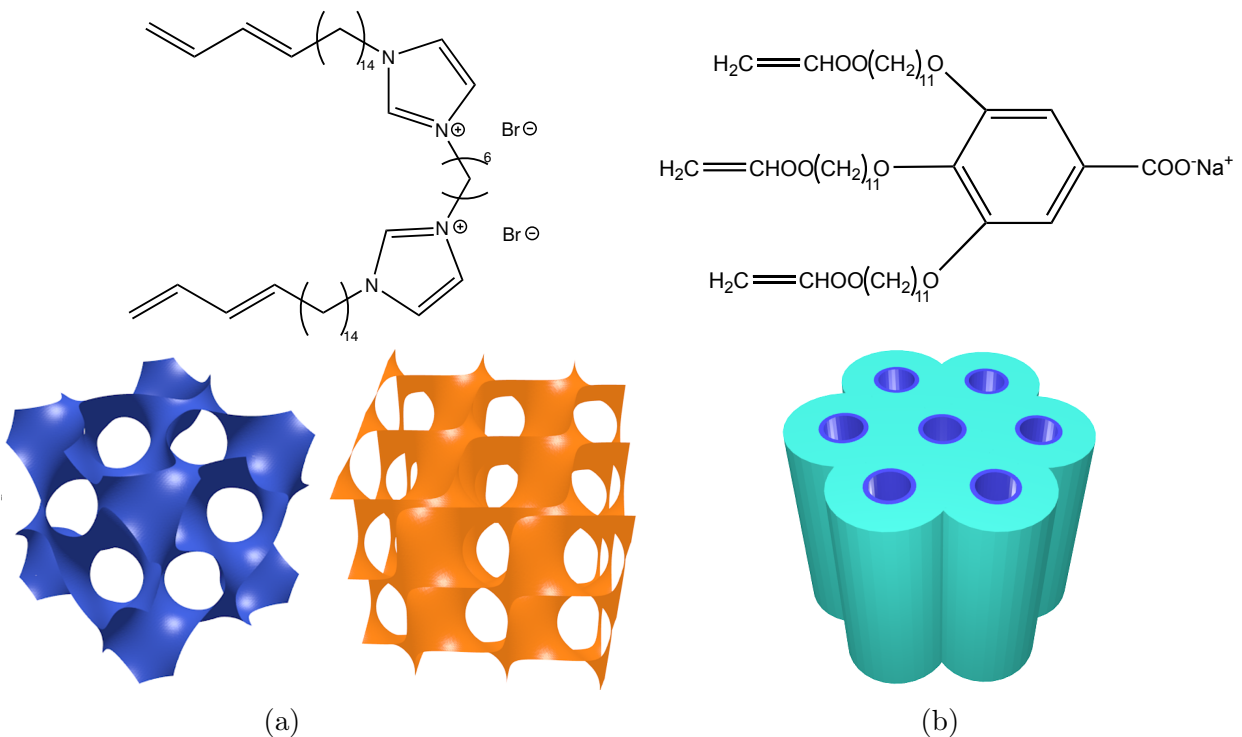


Figure 1: The choice of LLC monomer and solvent leads to different accessible liquid crystalline phases. The monomer shown in (a) forms the  $Q_I$  phase in either the  $Ia3d$  (left) or  $Pn3m$  (right) space group. The surfaces shown represent the interface between the hydrophilic and hydrophobic regions of the unit cell. As pictured, we assume that each region occupies an equal volume. The monomer shown in (b) will form the hexagonal columnar phase ( $H_{II}$  in the presence of water or  $Col_h$  when no water is present). The blue region represents the hydrophilic pores while the cyan region represents the surrounding hydrophobic monomer tails.

Recently, researchers have learned how to macroscopically align the hexagonal domains which has revived research into H<sub>II</sub> phase LLC membranes. Previously, research efforts were focused on the Q<sub>I</sub> phase, whose geometry does not require alignment. In 2014, Feng et al. showed that one can align Col<sub>h</sub> hexagonal domains using a magnetic field with subsequent cross-linking to lock the structure in place.<sup>11</sup> In 2016, Feng et al. showed that one could obtain the same result using a second technique termed soft confinement.<sup>13</sup> Current efforts are focused on extending the method to the H<sub>II</sub> phase and characterizing the performance of these newly aligned systems.

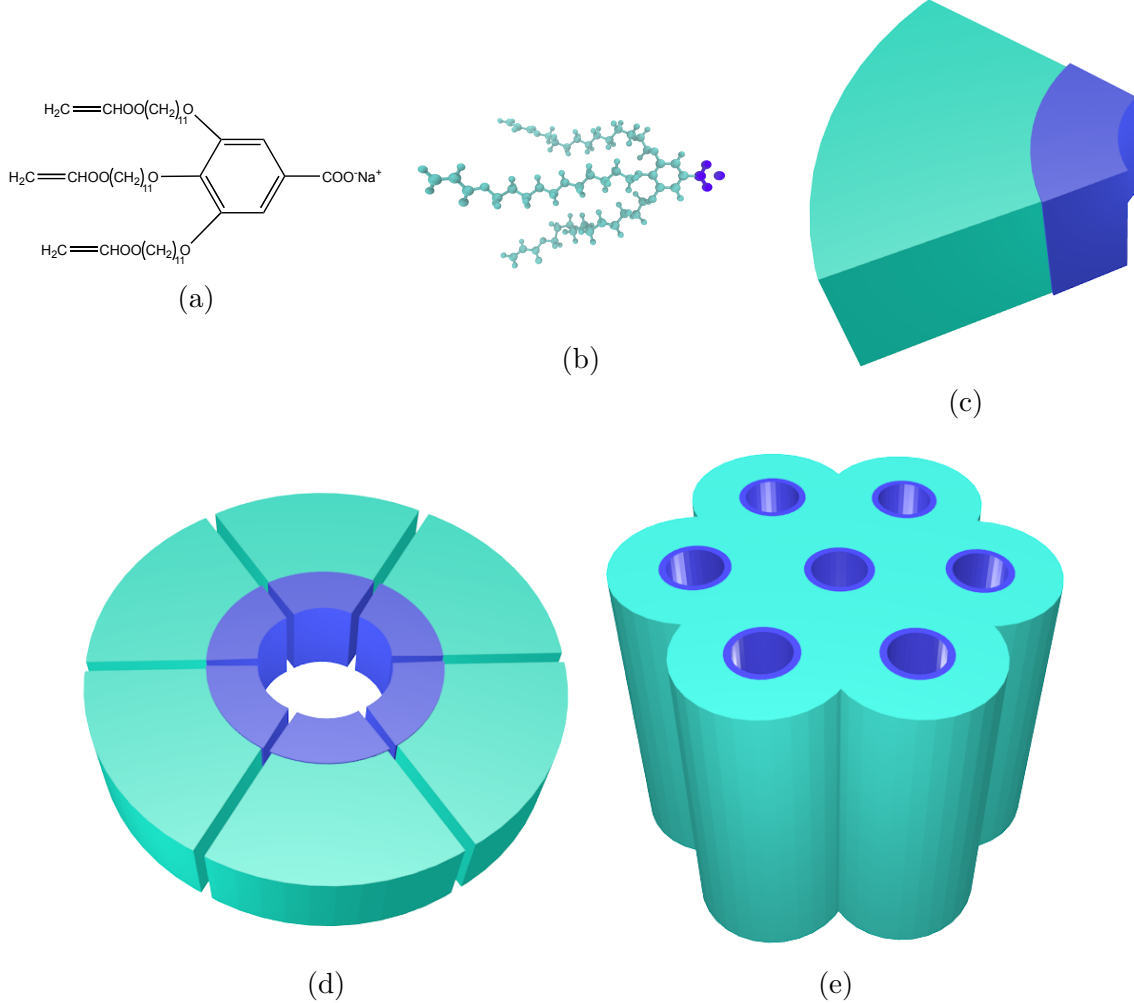


Figure 2: The LLC monomer Na-GA3C11 (a) rendered atomistically (b) exhibits wedge-like character (c). Monomer wedges assemble into disks (d) with hydrophilic head groups (blue) facing towards the disk center. The disks assemble into hexagonally packed columnar mesophases (e).

Our current understanding of the molecular details of LLC membrane nanostructure is not sufficient able to precisely design them for specific separations. Over the past 20 years, H<sub>II</sub>-phase LLC polymer membrane studies have been limited primarily to Na-GA3C11 with some characterization done after minor structural modifications. Resel et al. varied the length of the monomer tails and the counterion used and observed its affect on pore spacing.<sup>14</sup> In a later study of rejection performance, it was shown that membranes formed by cross-linked Na-GA3C11 in the H<sub>II</sub> phase cannot separate solutes less than 1.2 nm in diameter because the pores are too large.<sup>6</sup> We do not yet understand how to controllably reduce the effective pore size or how to tune the chemical environment in the nanopores of this or related materials for small molecule separations. The only source of predictive modeling for LLC systems have been macroscopic models that likely do not adequately describe transport at these length scales.<sup>8</sup> It will be challenging to efficiently narrow down the large design space in a laboratory setting without a robust model.

A molecular-level understanding of LLC polymer membrane structure, enabled by molecular dynamics (MD) simulations, can provide guidelines to reduce the large chemical space available to design monomers for creation of separation-specific membranes. A good molecular model should incorporate a detailed picture of the nanoscopic pore structure which will be crucial to understanding the role of monomer structure in solute transport and membrane design. Models resulting from molecular dynamics simulations will provide the required level of detail (Fig. 3), assuming the force fields are sufficiently accurate. With such an atomistic model, we can directly observe molecular-level solute transport and suggest governing mechanisms. We can observe how the choice of head group interacts with solutes of interest. We can interchange counterions which may influence both the pore size and the strength of the Donnan potential

In this study, we build a significantly more realistic atomistic model of LLC membranes than, to our knowledge, has ever previously been created, and explore what new structural information can be gained and what structure hypotheses are supported by this model. We

validate the model using as much experimental information as possible. We are most interested in reproducing the conclusions about structure drawn from small angle X-ray scattering (SAXS) and wide angle X-ray scattering (WAXS) experiments as well as in matching ionic conductivity measurements.<sup>13</sup>

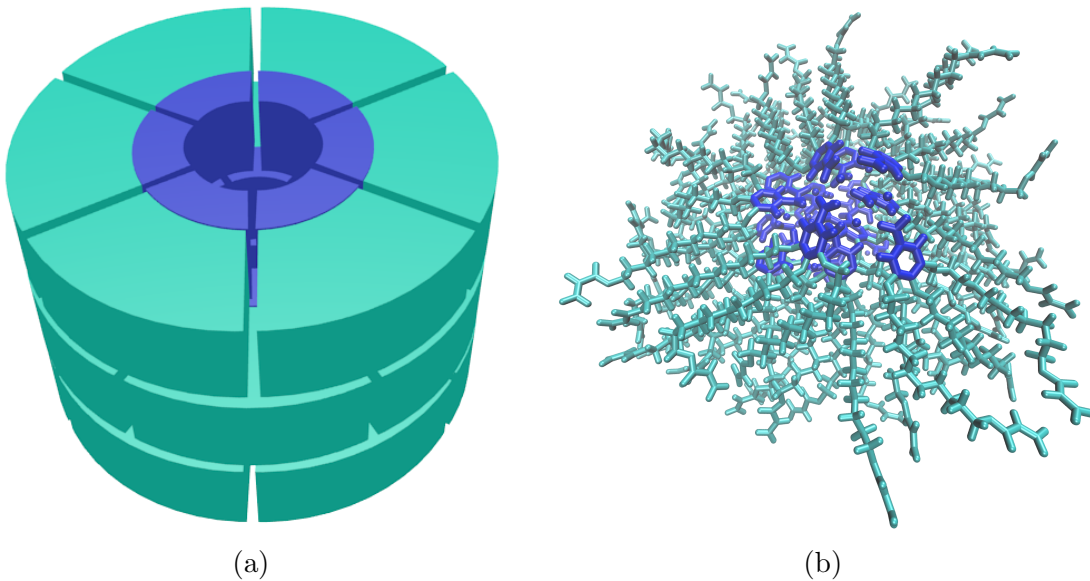


Figure 3: We can only speculate about solute behavior inside the membrane pores based on our previous picture of the pore structure (a). We will use a detailed molecular model in order to appropriately model the pore’s complex architecture which is crucial to understanding the mechanism of solute transport (b). The head group region is colored blue and the tail region is colored cyan in both representations.

Here we develop a model of the Col<sub>h</sub> assembly formed by Na-GA3C11. Compared to the H<sub>II</sub> phase, the Col<sub>h</sub> phase is a simpler starting point. The system has no water which will allow us to simulate longer timescales, and there exists detailed experimental characterization of the fully aligned state, including 2D wide-angle X-ray scattering (WAXS) patterns which are useful for reconstructing structural data. We anticipate using this Col<sub>h</sub> model in order to build an H<sub>II</sub> model in the future.

In order to appropriately model transport in these ordered, nanoporous organic systems, we must first gain a thorough understanding of the nanoscopic structure of LLC polymer

membranes. Our current level of understanding about the structure at the nanoscale is limited. Using X-ray diffraction and TEM data we can infer that monomers aggregate into hexagonally packed columns with their head groups facing towards the column center. There remain several key questions that we will investigate in order to expand this understanding:

1. *If layers do exist, how many monomers constitute a single layer?* A simple molecular simulation study of a similar molecule suggested that there are 4 monomers in each layer.<sup>15</sup> Their model likely does not sufficiently imitate the chemical environment present in the real system since it only contains 16 total monomers. A separate calculation for NA-GA3C11, based on the estimated volume of the liquid crystal monomers, proposes that each layer consists of seven monomers.<sup>14</sup> Our best chance to answer this question is by using a molecular model orders of magnitude larger than any other reported atomistic liquid crystal membrane simulation, as we present here. We will directly change the layer composition and note its effect on membrane structure.
2. *How do monomers in each layer position themselves with respect to surrounding layers?*  $\pi$ - $\pi$  stacking interactions between aromatic monomer head groups may be a driving force of self-assembly in this system.<sup>16</sup> Gas phase *ab initio* studies of benzene dimers have shown a clear energetic advantage for parallel displaced and T-shaped  $\pi$ - $\pi$  stacking conformations over a sandwiched conformation.<sup>17</sup> Substituted benzene rings exhibit an even stronger  $\pi$ - $\pi$  stacking attraction which favors the parallel displaced configuration in all cases except where the substitutions are extremely electron withdrawing.<sup>18,19</sup> In this study, we compare simulated X-ray diffraction patterns to experiment in order to deduce which stacking configuration is most likely. We also dive deeper into the origin of features present in the 2D diffraction patterns.
3. *Does our model support the existence of layers and if so, how well defined are the layers?* Indications of strong  $\pi$ - $\pi$  stacking interactions in the direction perpendicular to the membrane plane, combined with the wedge-like character of the LLC monomers,

suggests that monomers should arrange into disks that stack in layers.  $\pi$ - $\pi$  stacking will only occur between the aromatic monomer head groups which leaves no description of what is happening in the monomer tail region. The tails may entangle isotropically while maintaining stacking order among headgroups.

4. *Can the system exist in other metastable states or phases that are not accessed during experiments?* There remains the possibility that there is more than one metastable state associated with a given LLC phase. Simulating a membrane atomistically requires many atoms which limits the timescales accessible with MD. It is reasonable to expect that we will generate configurations which are kinetically trapped in a metastable free energy basin. We must be able to identify which states are most consistent with experiment.
5. *What constitutes a pore, and what are the details of its pore architecture?* The limited picture that experiment provides tells us that there are hexagonally packed, hydrophilic regions where transport is likely to occur. One may instinctively assume that these regions are hollow tube-like pathways. We will explore the composition of the pores and the partition between the hydrophilic and hydrophobic regions.
6. *Is it necessary to include any water in order to appropriately model the Col<sub>h</sub> phase?*

While past work describes the Col<sub>h</sub> phase as dry,<sup>11</sup> it has been suggested by experimentalists, in unpublished communications, that it is likely that neat monomer leaches small amounts of ambient water. Experimentally, achieving a hexagonal phase with a completely dry system has proven difficult. If neat monomer sits in ambient conditions, its color turns from transparent to slightly opaque and a hexagonal phase forms. Although we will not explore whether water is necessary for self-assembly, we hypothesize that the hydrogen bonding network formed by the water may play a role in structuring the pores and holding together the hexagonal phase. We can look at correlation functions and use simulated X-ray diffraction patterns to see if there is any

meaningful structural difference between a “dry” and “wet” system.

We used experimental small-angle X-ray scattering (SAXS) data from<sup>13</sup> (Fig. 4a) and wide angle X-ray scattering (WAXS) data (Fig. 4b, produced as described in<sup>11</sup>) for comparison to our model. We rely primarily on the 2D WAXS data since it encodes all structural details down to the sub-nm scale. There are five major features of interest present in the 2D experimental pattern shown in Figure 4b.

1. *R-π*: The location of the first is at  $q_z = 1.7 \text{ \AA}^{-1}$ , corresponding to a real space separation of 3.7 Å. Previous work<sup>11</sup> attributes this reflection to  $\pi$ - $\pi$  stacking between aromatic rings in the direction perpendicular to the membrane plane, or z-axis.<sup>11</sup> For simplicity, we will refer to this reflection as R- $\pi$ .
2. *R-helix*: A weak intensity line, located at exactly half the  $q_z$  value of R- $\pi$  ( $q_z = 0.85 \text{ \AA}^{-1}$ ), corresponds to a real space periodic spacing of 7.4 Å. This reflection has been interpreted as  $2_1$  helical ordering of aromatic rings along the z axis,<sup>11</sup> meaning that if one traces the positions of the aromatic rings with a helical curve, then for each full turn in the helix, one will encounter two aromatic rings. For this reason we will refer to reflection as R-helix.
3. *R-alkanes*: A low intensity ring located at  $r = 1.4 \text{ \AA}^{-1}$  marks the third major reflection of interest. The real space separation corresponds to 4.5 Å which is characteristic of the average spacing between packed alkane chains.<sup>20</sup> We will call this reflection R-alkanes.
4. *R-spots*: Within R-alkanes, are four spots of higher relative intensity. Accordingly, we name these reflection R-spots. The location of all spots is  $\sim 37^\circ$  from the  $q_z$  axis in their respective quadrants. In many liquid crystal systems one can explain the spots as the tilt angle of the alkane chains with respect to the membrane plane.<sup>21</sup>
5. *R-pores*: The final feature corresponds to the spacing and symmetry of the  $d_{100}$  plane. This plane is geometrically related the distance between pores. The feature, which we

named R-pores, is characterized by dots along the equatorial axis defined when  $q_z = 0$ . The spacing between dots is indicative of the hexagonal symmetry of the packed pores. We observe the same information with higher resolution using SAXS (Fig. 4a).

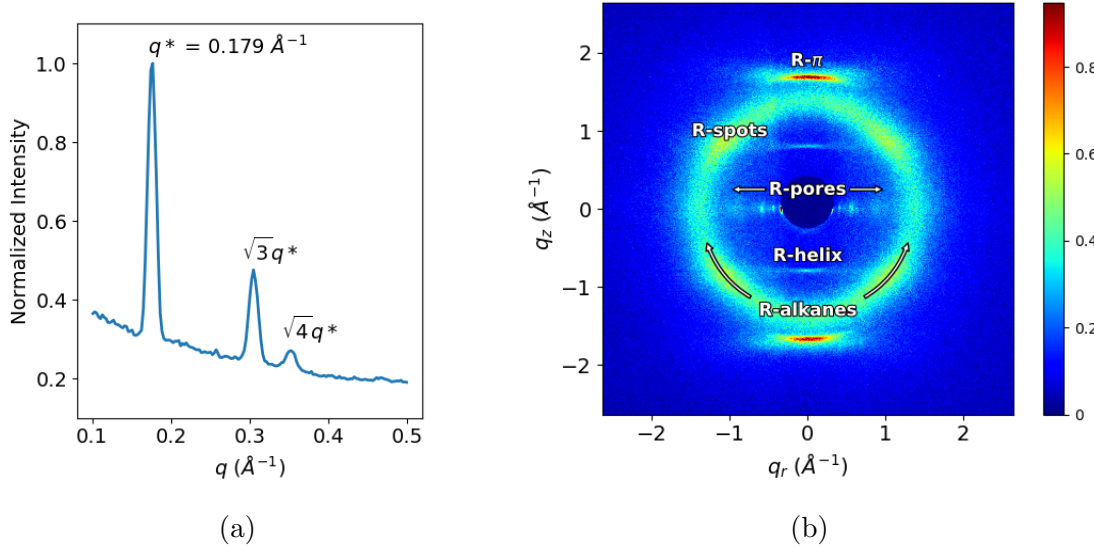


Figure 4: (a) (Reproduced from<sup>13</sup>) The repeat spacing in the 1D small angle X-ray scattering pattern is characteristic of hexagonal packing. The leading peak,  $q^*$ , represents the distance between the  $d_{100}$  planes. Using this distance, we know that the distance between pore centers is 4.12 nm. (b) 2D WAXS gives details about repeating features on the order of angstroms. Experimentalists have explained each of the 5 major reflections present as follows: (R- $\pi$ ) Aromatic head groups  $\pi - \pi$  stack 3.7  $\text{\AA}$  apart. (R-helix) Monomers arrange vertically in a  $2_1$  helix. (R-alkanes) Alkane chain tails pack 4.5  $\text{\AA}$  apart. (R-spots) Monomer tails are tilted with respect to the membrane plane. (V) As derived from SAXS, the pores are spaced 4.12 nm apart and pack hexagonally

## Methods

### Monomer Parameterization

We parameterized the liquid crystal monomers using the Generalized AMBER Force Field<sup>22</sup> with the Antechamber package<sup>23</sup> provided with AmberTools16.<sup>24</sup> We assigned atomic charges using the am1bccsym method of `molcharge` shipped with QUACCPAC from Openeye Scientific Software. We ran all molecular dynamics simulations using Gromacs 2016.<sup>25-28</sup>

We generated an ensemble of characteristic, low-energy vacuum monomer configurations by applying a simulated annealing process to a parameterized monomer. We cooled monomers from 1000K to 50K over 10 nanoseconds. We randomly pulled a low energy configuration from the trajectory then reassigned charges using `molcharge`. Using the new charges, we annealed the monomer system again and pulled a random monomer configuration from the trajectory which we used for full system construction (Figure 5a). See Supporting Information for further detail.

## Unit Cell Preparation

The timescale for self-assembly of monomers into the hexagonal phase is unknown and likely outside of a reasonable length for an atomistic simulation, calling for a more efficient way to build the system. Previous work has shown a coarse-grained model self assemble into the H<sub>II</sub> phase configuration in  $\sim$ 1000 ns.<sup>29</sup> We attempted atomistic self-assembly by packing monomers into a box using Packmol.<sup>30</sup> Simulations of greater than 100 ns show no indicators of progress towards an ordered system. To bypass the slow self-assembly process, we use Python scripts to assemble monomers into a structure close to one of a number of hypothesized equilibrium configurations (Figure 5).

A typical simulation volume contains four pores in a monoclinic unit cell, the smallest unit cell that maintains hexagonal symmetry when extended periodically. Each pore is made of twenty stacked monomer layers with periodic continuity along the pore axis, avoiding any edge effects and creating an infinite length pore ideal for studying transport. We prefer a small number of layers in order to reduce computational cost and to allow us to look at longer timescales. Ultimately, we chose to build a system with 20 monomer layers in each pore in order to obtain sufficient resolution when simulating X-ray diffraction patterns.

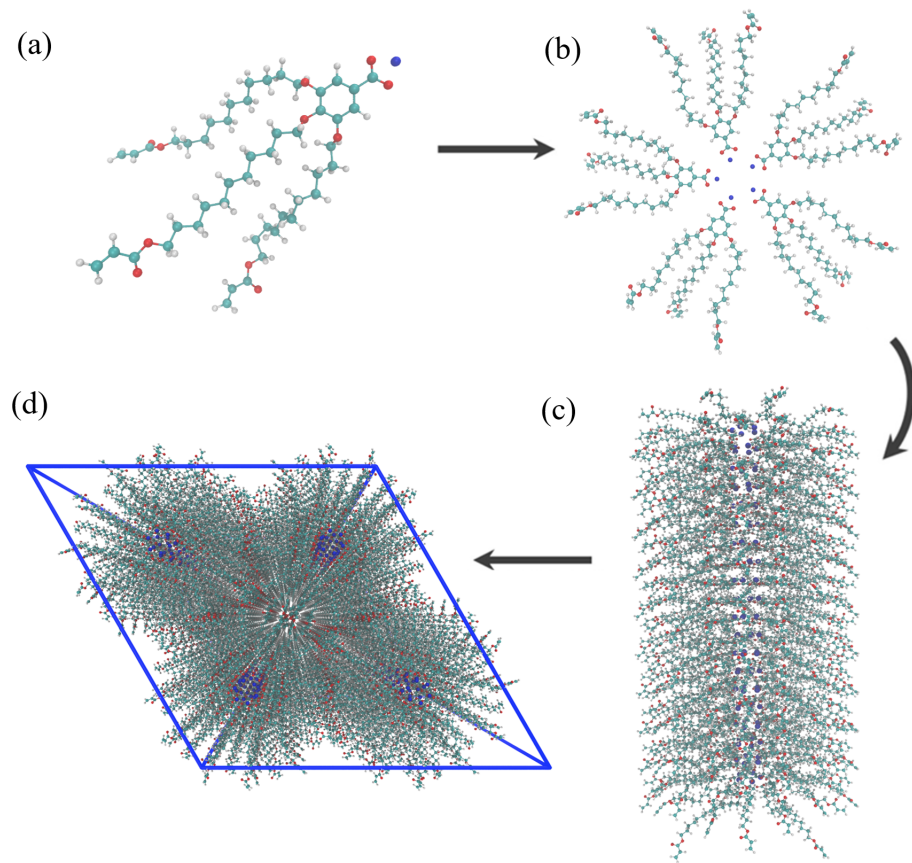


Figure 5: (a) We parameterized a single monomer and annealed it to produce a low energy configuration. (b) A Python script rotates and assembles monomers into layers with hydrophilic centers. (c) We chose to stack twenty layers on top of each other to create pores. (d) The pores are duplicated and placed into a monoclinic unit cell.

## Monomer Placement

When constructing an initial configuration, there are a number of variables which require careful consideration while placing monomers. The equilibrium configuration is sensitive to some while insensitive to others. The starting pore radius, defined as the distance of a chosen head group carbon from the pore's central axis, does not influence the equilibrium structure if one chooses a reasonable value. The pore radius is chosen to be 0.5 nm in our initial configurations. The initial distance between pores, within a wide range, also has little effect on the equilibrated structure. However, one should not start them too close or there will be high energy repulsions during early equilibration. We chose an initial pore spacing of 4.5 nm,  $\sim$ 10% larger than the experimental value of 4.12 nm. A sensitivity analysis of both parameters is presented in the Supporting information. The distance between layers, the rotation of the layers with respect to adjacent layers, and the number of monomers per layer do influence the equilibrium structure and require further justification for their choices. We rely on experimental data to inform them.

We chose the layer spacing for the initial configuration based on R- $\pi$  and then allowed the system to readjust during equilibration. Each monomer was rotated so the plane of its aromatic head groups would be coplanar with the xy plane. We explored three different initial layer spacings. The first is exactly equal to R- $\pi$  with layers placed so aromatic rings stack 3.7 Å apart in the z-direction. We explore a second system with an initial layer spacing of 5 Å. We briefly explored a third system with an initial layer spacing of 10 Å, however it shows non-physical behavior which is detailed in the Supporting Information.

We chose the relative interlayer orientation based on clues from diffraction data as well as the various known stacking modes of benzene and substituted benzene rings: sandwiched, parallel-displaced and T-shaped.<sup>17</sup> We ruled out the T-shaped configuration because its  $\sim$ 5 Å equilibrium stacking distance<sup>17</sup> is inconsistent with R- $\pi$ . It is also infeasible for the monomers to orient in the T-shaped conformation because of the bulky tail groups. We will explore the system's preference towards the sandwiched vs. parallel displaced stacking

modes in some detail. Both have reported stacking distances near the  $R-\pi$  value of 3.7 Å. Headgroups in our sandwiched initial configuration stack directly on top of each other while headgroups in the parallel displaced initial configuration stack with an offset of  $180^\circ/n_{mon}$  where  $n_{mon}$  is the number of monomers per layer. See the Supporting Information for a detailed illustration of the initial configurations in each mode.

The number of monomers in each layer is unknown, as stated in question (1). We tested configurations constructed with a varied number of monomers per layer. We built systems in the offset and parallel displaced configurations with 4, 5, 6, 7 and 8 monomers per layer.

## Equilibration

We developed equilibration schemes to create dry and wet configurations. Both schemes start with an initial configuration generated according to the previous guidelines. To create a dry configuration, we fix monomer head groups in the sandwiched or parallel-displaced configuration using position restraints with a force constant of  $10^6$  kJ mol $^{-1}$  nm $^{-2}$ . We run a 50 ps simulation in the NVT ensemble which allows the monomer tails to settle without disrupting the ordering of the head groups. Doing so also mitigates system dependence on initial monomer configuration. Every 50 ps, we reduce the force constants by the square root of its previous value. Once the force constant is below 10 KJ mol $^{-1}$  nm $^{-2}$ , we reduce the restraints in a sequence with values of 8, 3, 2, 1, and 0 KJ mol $^{-1}$  nm $^{-2}$  respectively. We allow the resulting unrestrained structure to equilibrate for 5 ns in the NPT ensemble with pressure controlled by the berendsen barostat. Next, we run long NPT equilibration simulations for at least 400 ns using the Parrinello-Rahman barostat with a time constant of 10 ps.

In order to create a “wet” system, we solvated an initial configuration with water using `gmx solvate`. We remove all water molecules placed outside the pore region. Then we randomly remove water molecules inside the pore region until the pores reach the desired concentration of water. The remainder of the equilibration follows the same procedure as

the dry system.

## Cross-linking

In order to fully match synthetic procedures, we created a cross-linking algorithm that one can apply to equilibrated structures. The purpose of cross-linking is to maintain macroscopic alignment of the crystalline domains, ensuring aligned, hexagonally packed pores. For that reason, we are not concerned with replicating the kinetics of the reaction, but instead emphasize the consistency of the final structure with experimental structural data.

We developed the algorithm based on the known reaction mechanism. Cross-linking of this system is a free radical polymerization (FRP) taking place between terminal vinyl groups present on each of the three monomer tails. FRPs require an initiator which bonds to the system, meaning new atoms are introduced into the system. For simplicity, we simulated the initiator as hydrogen and made it present in the simulation by including them as dummy atoms in all possible locations where an addition could occur. We carry out the cross-linking procedure iteratively. During each iteration, the algorithm selects eligible bonding carbon atoms based on a distance cut-off. The topology is updated with new bonds and dummy hydrogen atoms are changed to appropriate hydrogen types. Head-to-tail addition was the only propagation mode considered due to its dominance in the real system.<sup>31</sup> We did not consider direction of attack because the resultant mixture is racemic.

Our implementation requires long simulation times to achieve high cross-link densities. A typical cross-linking procedure can take up to 24 hours. In order to collect equilibrated data, further NPT simulation is necessary. We typically run a cross-linked system for an additional 100 ns to allow the system to readjust. For those reasons we did not cross-link all systems tested, but only the most promising structure. We show that cross-linking does not significantly change any of our drawn conclusions in Section 3.6.

## Equilibrium Calculations

### *Determining equilibration time*

Using equilibrated structures, we carry out various calculations to characterize the system. We define the point at which a system is equilibrated based on when the distance between pores stops changing. We determined when the distances stopped changing by applying the statistical test, `pymbar.timeseries.detectEquilibration`, to the time series.<sup>32,33</sup> Simulations of 400 ns give at least 50 ns of equilibrated simulation trajectory.

### *Calculation of pore spacing*

To calculate the equilibrated pore spacing, we measured the distance between pore centers. We located the pore centers by averaging the coordinates of sodium ions in their respective pores. We generated pore spacing statistics using the bootstrapping technique (See Supporting Information).

### *The nematic order parameter*

We calculated the nematic order parameter for our system in order to understand the degree of ordering among monomer head groups. Typically, the nematic order parameter is calculated for nematic liquid crystal systems which are characterized by unidirectional ordering of liquid crystal monomers. The preferred direction of monomers is defined by the unit director vector, **n**. Assuming a single preferred direction of alignment, the nematic order parameter,  $S$ , is defined as:

$$S = \frac{1}{2} \langle (3 \cos^2 \theta - 1) \rangle \quad (1)$$

where  $\theta$  is the angle between the molecular long axis and **n**. In a perfectly ordered system, the molecular axis should be aligned with **n** and give an order parameter of  $S = 1$ . We are interested in quantifying the degree of monomer head group alignment between systems. We use Eq. 1 to accomplish this by defining **n** as the z-axis (or pore axis), and then measuring

the angles,  $\theta$ , between  $\mathbf{n}$  and the vectors perpendicular to the plane of the aromatic head groups. See the Supporting Information for a diagram.

### ***Pair distribution functions***

The normalized pair distribution function,  $g(\mathbf{r})$ , describes the probability of finding a pair of particles separated by  $\mathbf{r}$ ,

$$g(\mathbf{r}) = \frac{1}{\rho N} \left\langle \sum_{i=1}^N \sum_{j \neq i}^N \delta(\mathbf{r} + \mathbf{r}_j - \mathbf{r}_i) \right\rangle \quad (2)$$

where  $\rho$  is the average number density of particles and  $\delta(\mathbf{r})$  is the Dirac delta function.<sup>34</sup>

We applied equation 2 in three dimensions and then extracted one and two dimensional distribution functions by collapsing the grid along the appropriate axes.

In the 1D case, we measured the pair distribution function between centers of masses of aromatic head group rings,  $g(z)$ , along the z-axis (perpendicular to the membrane plane). To extract the average distance between layers we applied a discrete Fourier transform to  $g(z)$  and extracted the highest intensity frequency. We performed the same procedure to calculate  $g(z)$  of the tails except instead of using the center of masses of the tails, we averaged  $g(z)$  for each atom that makes up the tail.

In two dimensions, we observed xy and xz pair distribution functions based on the center of masses of the aromatic head group rings. For the xy pair distribution functions, we used a rotated frame of reference. For a given center of mass, we rotated the coordinates so that the vector created from the center of mass to the pore center was aligned with the positive x-axis.

### ***Radial distribution functions***

Closely related to the spatial correlation functions, we explored the pores' compositions by measuring the average number densities of various monomer components as a function of

distance from the pore centers. We looked at the average number density of sodium ions, aromatic rings and carbon atoms making up the monomer tails. We binned the radial distance of all atoms in each group from the pore centers, then normalized by the volume of the annulus defined by the bin edges and the z box vector (See Supporting Information for a diagram).

### ***Simulated structure factor calculations***

This section replaced by Yelk/Glaser text. Simulated X-ray diffraction patterns are generated based on atomic coordinates in order to make a direct experimental comparison. All atomic coordinates were simulated as Gaussian spheres of electron density corresponding to each atom's atomic number. A three dimensional Fourier transform (FT) of the array of electron density results in a three dimensional structure factor which represents the unit cell in reciprocal space. We matched experimental 2D WAXS patterns by adjusting the initial spacing between layers and the orientation of the head groups with respect to adjacent layers.

We normalized the colorbars on all diffraction patterns relative to R-alkanes. We believe that the alkane-alkane density, averaged over all angles, is the feature most likely to be replicated between experiment and simulation. Other features are dependent on system ordering which is likely to have some dependence on initial configuration. We calculated the average intensity within R-alkanes of the experimental pattern,  $I_{avg}$ . We exclude intensities within  $\pm 30^\circ$  of the meridional axis defined by  $q_r = 0$ , since the simulated patterns differ from experiment in those regions in all cases. Specifically, in contrast to the experimental WAXS pattern, R- $\pi$  appearing in simulated diffraction patterns intersects with R-alkanes (See Fig. 7). We multiplied  $I_{avg}$  by a scaling factor,  $f$ . Intensities that appear in the experimental pattern  $\geq f \times I_{avg}$  are colored uniformly. We apply the same scaling method to the simulated patterns. We carefully chose a scaling factor of  $f = 3.1$  in order to (1) visibly display all features in the experimental pattern and (2) to allow us to compare the

relative intensities of features between simulated and experimental diffraction patterns.

### ***Ionic conductivity calculations***

We calculated ionic conductivity using two different methods for robustness. The Nernst-Einstein relation, relates the DC ionic conductivity,  $\sigma$ , to ion diffusivity,  $D$ , concentration,  $C$ , ion charge,  $q$ , the Boltzmann constant,  $k_b$ , and temperature,  $T$ :

$$\sigma = \frac{q^2 C D}{k_b T} \quad (3)$$

We measured sodium ion diffusion coefficients by calculating the slope of the linear region of the z-direction mean square displacement curve as indicated by the Einstein relation.<sup>35</sup> We visualized the MSD plot to determine where to begin and end a linear fit. We measured ion concentration with respect to the volume of the entire unit cell. The second method, termed the Collective Diffusion model, measures the movement of the collective variable,  $Q$ , which is defined as the amount of charge transfer through the system and can be thought to represent the center of charge of the system. The conductance,  $\gamma$ , of the system can be calculated as:

$$\gamma = \frac{D_Q}{k_b T} \quad (4)$$

We convert the resulting value to ionic conductivity by multiplying by channel length and dividing by the membrane cross sectional area.  $D_Q$  is the diffusion coefficient of the collective variable  $Q$ . It is calculated using the Einstein relation. One can access a detailed derivation of the model elsewhere.<sup>36</sup>

# Results and Discussion

## Structural Characterization

### Number of monomer per layer

Our simulations best support a model built with 5 monomers per layer based on the measured equilibrated pore-to-pore distances. To discern the composition of the monomer layers, addressing question (1), we ran simulations of systems created with 4–8 monomers per layer. We built systems in both the parallel displaced and sandwiched configurations with layers initially spaced 3.7 Å apart. We prepared equilibrated configurations according to the dry equilibration procedure. All systems are stable after 400 ns of simulation. In a sense, all systems are at least metastable, addressing question (4), however not all will make physical sense or fit the experimental profile that we are trying to match. Figure 6 shows the equilibrated pore-to-pore distances for all systems tested. Systems built with 5 monomers in each layer equilibrate to a pore spacing that is most consistent with the experimental value of 4.12 nm derived from SAXS measurements (Figure 4a). The remainder of this discussion will focus on the analysis of systems built with 5 monomers per layer.

### Relative interlayer head group orientation

We answer question (2) by simulating X-ray diffraction patterns produced from equilibrated MD trajectories. We tested systems built with 5 monomers per layer in the parallel displaced and sandwiched configurations. We generated simulated patterns using portions of simulation trajectory after equilibration. The patterns for both structures are shown and compared to experiment in Figure 7.

Simulated XRD of the sandwiched configuration contains all experimental features except for R-helix. R-alkanes, R-spots and R-pores appear close to their expected locations. R- $\pi$  is also present, however it intersects R-alkanes at a  $q_z$  value lower than experiment meaning the head groups in our model prefer to stack farther apart.

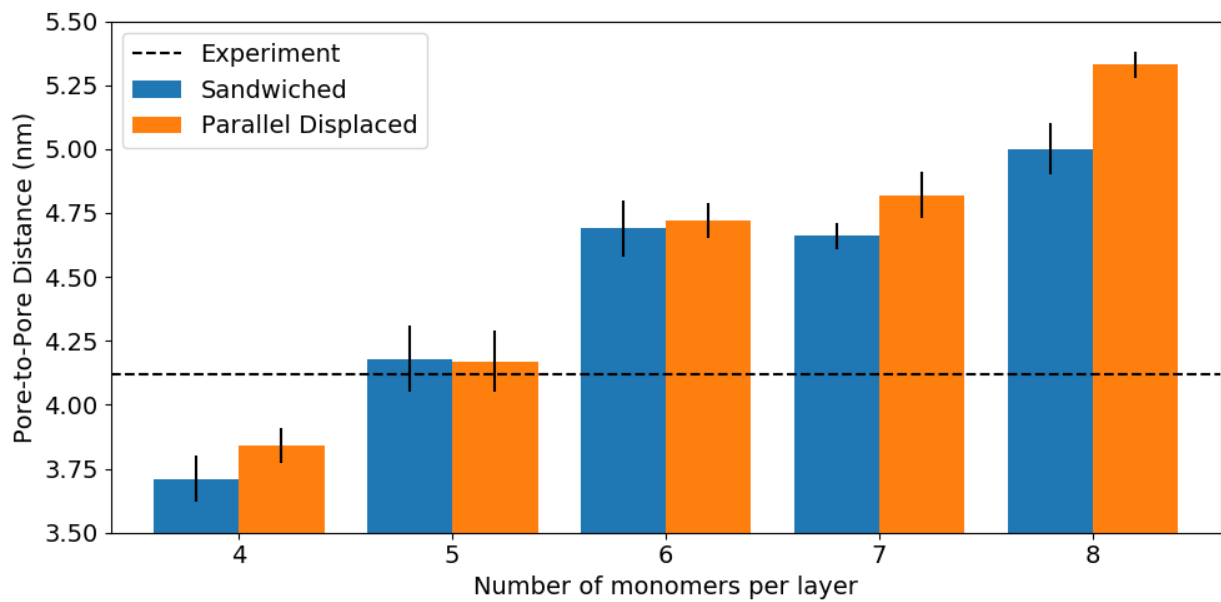


Figure 6: Systems with 5 monomers per layer have equilibrated pore spacing closest to the experimental value of 4.12 nm. The equilibrated pore spacing of the model increases as the number of monomers in each layer increases. The pore spacing of systems starting in the sandwiched configuration is systematically lower than those started in the parallel displaced configuration.

The parallel displaced configuration results in a simulated XRD pattern with the closest match to experiment. It produces the only pattern that exhibits all major reflections. R-alkanes and R-pores appear as they do in the sandwiched configuration. R-spots and R- $\pi$  appear, however with a lower intensity relative to R-alkanes when compared to the sandwiched configuration. R-helix appears due to the parallel displaced aromatic rings. It is a subharmonic of R- $\pi$  since the nearest vertically stacked head group to any given head group is  $2 \times R-\pi$  away.

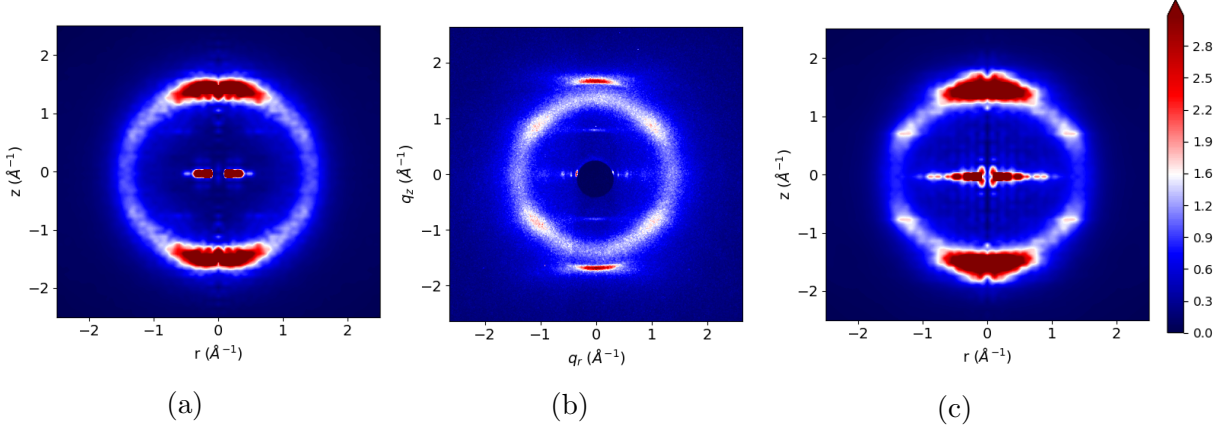


Figure 7: The simulated XRD pattern generated from the equilibrated trajectory of the parallel displaced configuration (a) exhibits all major reflections present in the experimental WAXS pattern (b). The simulated XRD pattern generated from the equilibrated trajectory in the sandwiched configuration (c) shows all major reflections except R-helix.

In both the parallel displaced and sandwiched configurations, we noted that R- $\pi$  appears in a location which corresponds to a real space separation larger than experiment. We attribute this discrepancy to GAFF's inability to appropriately model the aromatic interactions which would be necessary to achieve the correct  $\pi$ - $\pi$  stacking distance. The monomers in our model have bulky tails whose entropic contributions compete with the  $\pi$ - $\pi$  stacking interaction energy. There have been efforts to model systems that contain  $\pi$  interactions in a classical mechanical context using polarizable forcefields,<sup>37</sup> but they are significantly more computationally expensive to reach the time scales required to equilibrate these systems at the present time.

In addition to R- $\pi$  being shifted to lower  $\mathbf{q}$  values, a few factors combine to make the

simulated R- $\pi$  reflection visibly more intense than in the experimental pattern. The simplest reason is that R- $\pi$  and R-alkanes add together to boost the overall signal at intersecting values of  $\mathbf{q}$ . In addition, we observe a much higher maximum intensity within R- $\pi$ . The maximum intensity within R- $\pi$  of the normalized experimental pattern is 3.1, while the maximum intensity within R- $\pi$  of the normalized parallel displaced simulated pattern is 32.9. While direct numerical comparisons between simulation and experiment aren't necessarily precise due to underlying assumptions, an order of magnitude difference suggests some significance. We believe that we see such a high maximum for two reasons: (1) We are simulating a perfectly aligned system so all X-rays reflected along the pore axis would add constructively. The crystalline domains in the real system are not perfectly aligned (See azimuthal distribution in Supporting Information) which would lead to an overall decrease in the intensity of R- $\pi$ . (2) Our system is more ordered with high correlation between layers. We will come back to this point further in ensuing discussions.

There is a grid-like pattern near  $\mathbf{q} = 0$  which appears because the simulated system shows crystalline character. The grid features along nonzero values of  $q_z$  line up with reflections at  $q_z = 0$  which indicates positional correlations between columns in the z-direction. This type of correlation is expected for a crystalline material. If our system met the definition of a columnar liquid crystalline system, we should observe only weak short-range z-directional correlation within columns, with no correlation between columns.<sup>38</sup>

The R-spots signal, which appears in both simulated XRD patterns, is not a result of alkane chain tilt. Previous literature has attributed the spots in this particular WAXS pattern as the product of tilted alkane chains.<sup>11</sup> We looked closer at the sandwiched configuration since R-spots appears with the most strength in its simulated XRD pattern. We measured the tilt angle of the alkane chains and showed that our system equilibrates to an average tilt angle close to zero degrees (Fig. 8). To understand the origin of R-spots, we determined which atoms gave rise to the feature. Since R-spots is present as higher intensity spots within R-alkanes, it is likely that the spots arise as a consequence of the tails. By

removing all non-tail atoms from the trajectory and simulating a diffraction pattern, we were able to isolate the cause of the spots to the tails (Figure 9). Since the tails stay nearly flat, we plotted the centroids of the tails and measured the angle between each centroid and its nearest neighbors with respect to the plane of the membrane. We see distinct peaks in the distribution of these angles (Figure 10).

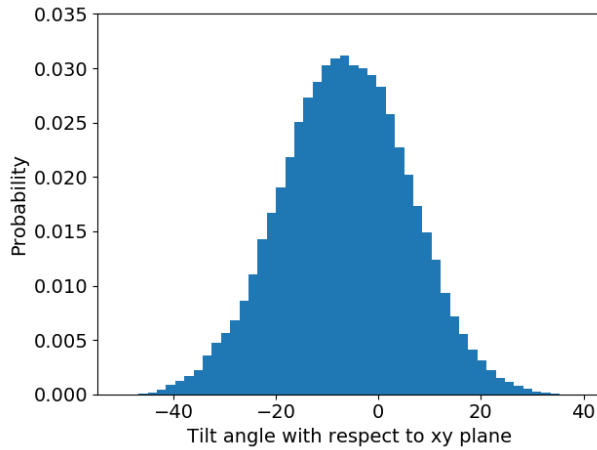


Figure 8: We measured the angle made between each monomer alkane tail and the membrane plane. The average tilt angle is near  $7^\circ$  which is far from the  $37^\circ$  tilt angle previously used to explain R-spots.

The peaks in the nearest neighbor angle distribution are consistent with the location of R-spots. The peaks of interest in Figures 10a and 10c are located at  $\pm 33^\circ$  which is the same location where the highest intensity of spots are located on the simulated patterns. We confirmed this conclusion by radially integrating the 2D WAXS pattern for  $|\mathbf{q}|$  values between 1.4 and 1.57 (between 4 and 4.5 Å in real space). We observe that distinct peaks appear ca.  $30^\circ$ , in close agreement with the previously measured angle distribution (Figs. 10b and 10d). We performed the same integration on the raw experimental data and found the angle at which R-spots reaches its highest intensity to be  $\pm 37^\circ$  which is a reconcilable difference with our simulated results.

The evidence supports the hypothesis that alkane chain tails pack in a hexagonal array. Groups of three tails associated with each monomer prefer to sit between tails of vertically

stacked monomers rather than stacking directly on top of them (Figure 11). This type of packing has been seen before in XRD studies of hydrocarbon chains.<sup>39</sup>

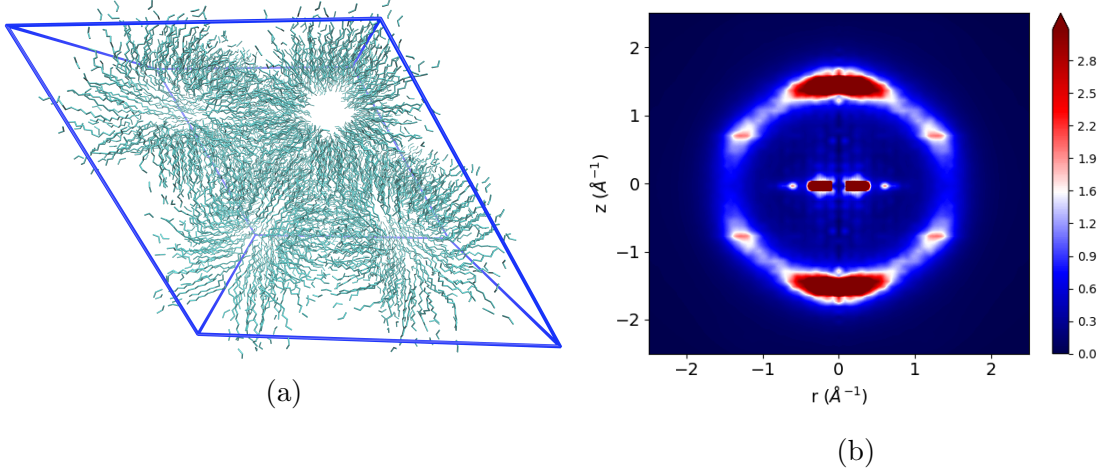


Figure 9: (a) We removed all atoms except carbon atoms that constitute the tails from a sandwiched configuration trajectory. (b) The simulated XRD pattern of the tail-only trajectory still shows R-spots

### Layer partitioning

In our simulations, layers are well-defined and persistent, answering question (3). We established our conclusion by plotting the two dimensional pair distribution function,  $g(y, z)$  of head group phenyl rings using Equation 2 (Figure 12). In both configurations, the phenyl rings stack in the  $z$ -direction, along  $y = 0$ , and clear layers are formed. The layers in the sandwiched configuration are more defined than those in the parallel displaced configuration and are strongly correlated with adjacent layers. We also observe correlation of layers between pores indicated by the non uniformity in  $g(y, z)$  in adjacent columns (along  $y = \pm 3.65$ ). Parallel displaced layers display weaker correlations but do not decay in their intensity as  $z$  increases. We do not see correlation between pores, however correlations within pores are strong throughout the length of the unit cell since there is no noticeable decay in layer intensity.

We plotted the one-dimensional pair distribution function,  $g(z)$ , for the phenyl rings and for carbon atoms that make up the monomer tails (Figure 13). The plots show clear periodic

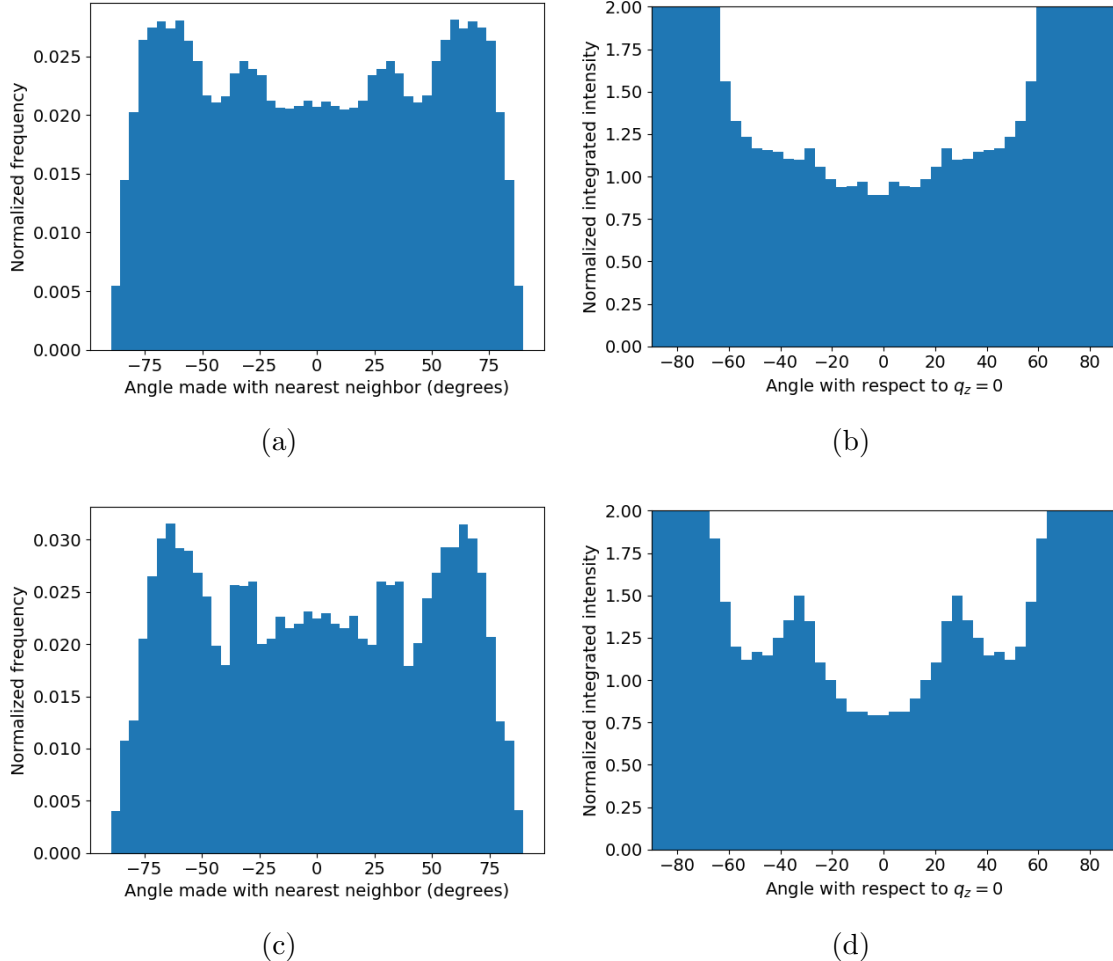


Figure 10: We hypothesize that R-spots is the result of ordered tail packing. Defining the membrane plane to be  $0^\circ$ , we measured the angles between each alkane chain tail centroid and its nearest neighbor centroids for the equilibrated parallel displaced (a) and sandwiched (c) configurations. Peaks that appear in each distribution are centered near  $\pm 33^\circ$ . We radially integrated the simulated XRD patterns of the parallel displaced and sandwiched configuration within the region bounding R-alkanes ((b) and (d) respectively). Peaks appear in the same location as the angle distributions which corroborates our hypothesis. Further, we note that the peaks are strongest in both plots associated with the sandwiched configuration. As shown in Figure 7c, systems simulated in the sandwiched configuration exhibit more intense R-spots reflections. Note that plots of integrated intensity are normalized so the average alkane intensity (excluding reflections  $\pm 30^\circ$  from the  $q_z$  axis) is set to 1. Plots are cut off for intensities greater than 2 so peaks are more visible.

maxima where layers are present. Layering is most pronounced in the head group region, however there is still a degree of layering that persists into the tail region. Using a Fourier

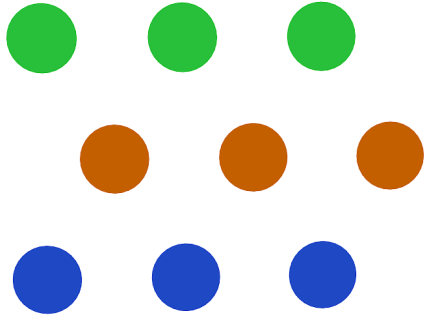


Figure 11: Monomer tails prefer to pack in a hexagonal array. Each circle represents a monomer tail as seen if viewed by looking from the end of the tail to the pore center. Each color represents distinct monomers from adjacent layers.

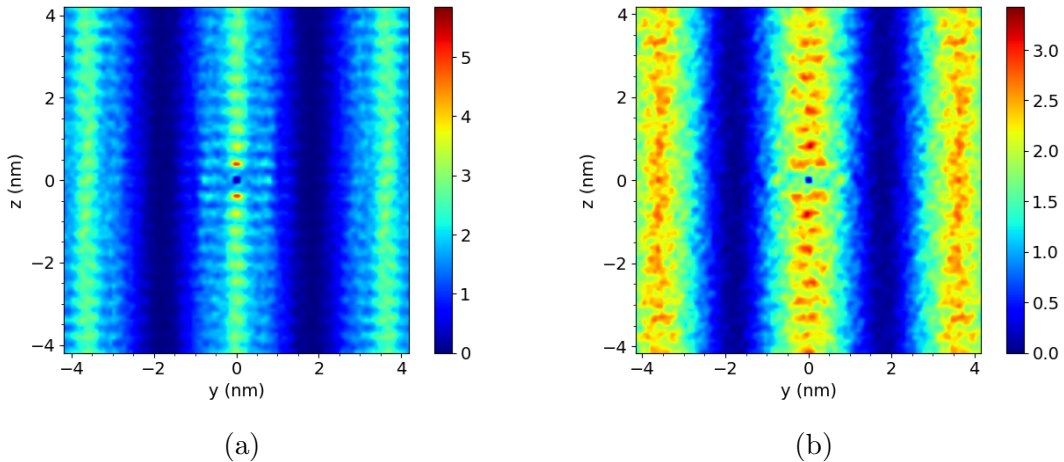


Figure 12: 2D pair distribution functions generated from systems built in the sandwiched (a) and parallel displaced (b) configurations, provide a more detailed picture of the pore structure in each. The sandwiched configuration

transform on  $g(z)$  from the head groups, we see that sandwiched configuration layers stack 4.39 Å apart while parallel displaced configuration layers stack 4.38 Å apart. Both stacking distances are in agreement with those observed in the simulated XRD patterns.

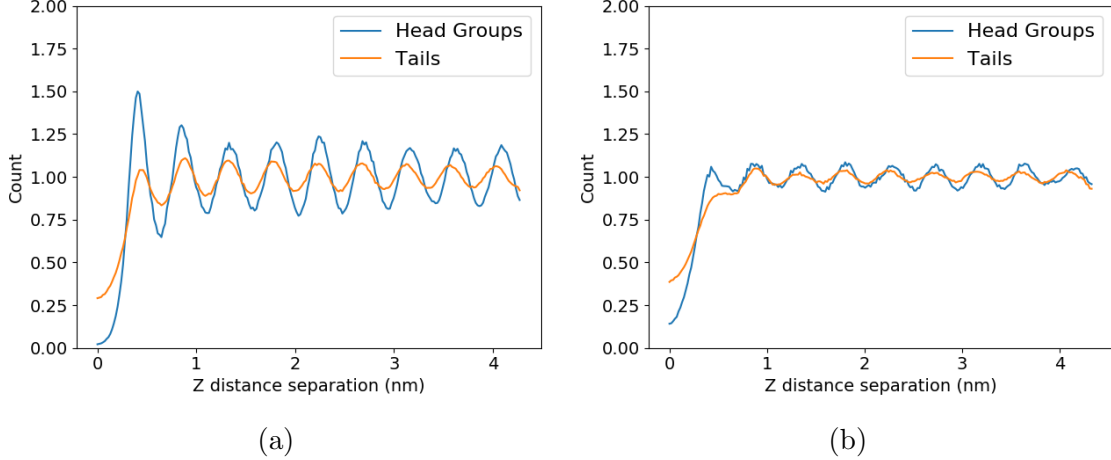


Figure 13: We support the existence of layers with the observance of clear periodic maxima in the  $z$ -direction pair distribution functions of the (a) 5 monomer per layer, sandwiched and (b) 5 monomer per layer, parallel displaced configurations. The extent to which we consider a system to be layered is based on the magnitude of the deviation of the periodic maxima from the average number density. The sandwiched configuration possesses a higher degree of layering than the parallel displaced configuration and, in both cases, the head group region has a higher degree of layer partitioning than the tail region. (See Supporting information for detailed definitions of the head group and tail regions)

### Initial Layer Spacing Affects System Equilibration

All systems up to this point were built with layers stacked 3.7 Å apart. When we build systems with layers stacked 5.0 Å apart and then let them equilibrate, we observe long-term stability of a qualitatively different configuration, suggesting that we have found another metastable free energy basin, further corroborating question (4). For reasons we will develop in the next segment of our discussion, configurations initially built with layers stacked 5.0 Å apart will be grouped into the disordered pore basin, while those built with layers initially stacked 3.7 Å apart will be grouped into the ordered pore basin.

The equilibrated pore spacing and distance between layers are different in the disordered pore basin. For both head group stacking arrangements, we observe an increase in the

equilibrated distance between layers (Fig. 14a) and a corresponding decrease in pore spacing (Fig. 14b).

The simulated X-ray diffraction patterns indicate further structural differences. In the parallel displaced configuration, almost all contrast between R-spots and R-alkanes fades (Figure 14c). In the sandwiched configuration, R-spots is present, but there are only two spots located at the intersection of  $q_z = 0$  with R-alkanes. (Figure 14d).

We quantified order in the z-direction by measuring the correlation lengths of all configurations. We measured the correlation length, L, by fitting  $g(z)$  using a non-linear least squares algorithm subject to a function of the form:

$$1 + A \sin(Bx + C) e^{-z/L} \quad (5)$$

where z is the independent variable and all other variables are fitting parameters. The correlation length for each system is given in Table 1.

Correlation lengths are shorter in the disordered pore basin than in the ordered pore basin. Layers in the ordered pore basin are strongly correlated with neighboring layers up to more than 10 layers away. This behavior deviates from experimental evidence. The experimental correlation length (See Supporting Information for details its derivation) suggests that layers are correlated with about 3 neighboring layers which is closer to the values exhibited by the disordered pore basin. We may need to simulate a system with many more layers in order to reduce the correlation contributed by periodic copies of the system.

We calculated the nematic order parameter for each system using Equation 1. The calculated values of S are presented in Table 1. The full distributions of angles between director  $\mathbf{n}$  and vectors orthogonal to monomer phenyl rings are presented in the Supporting Information. In general, ordered pore basin systems are more nematically ordered than disordered pore basin systems and sandwiched configuration systems are more nematically ordered than parallel displaced configuration systems. The head groups of the disordered pore basin have

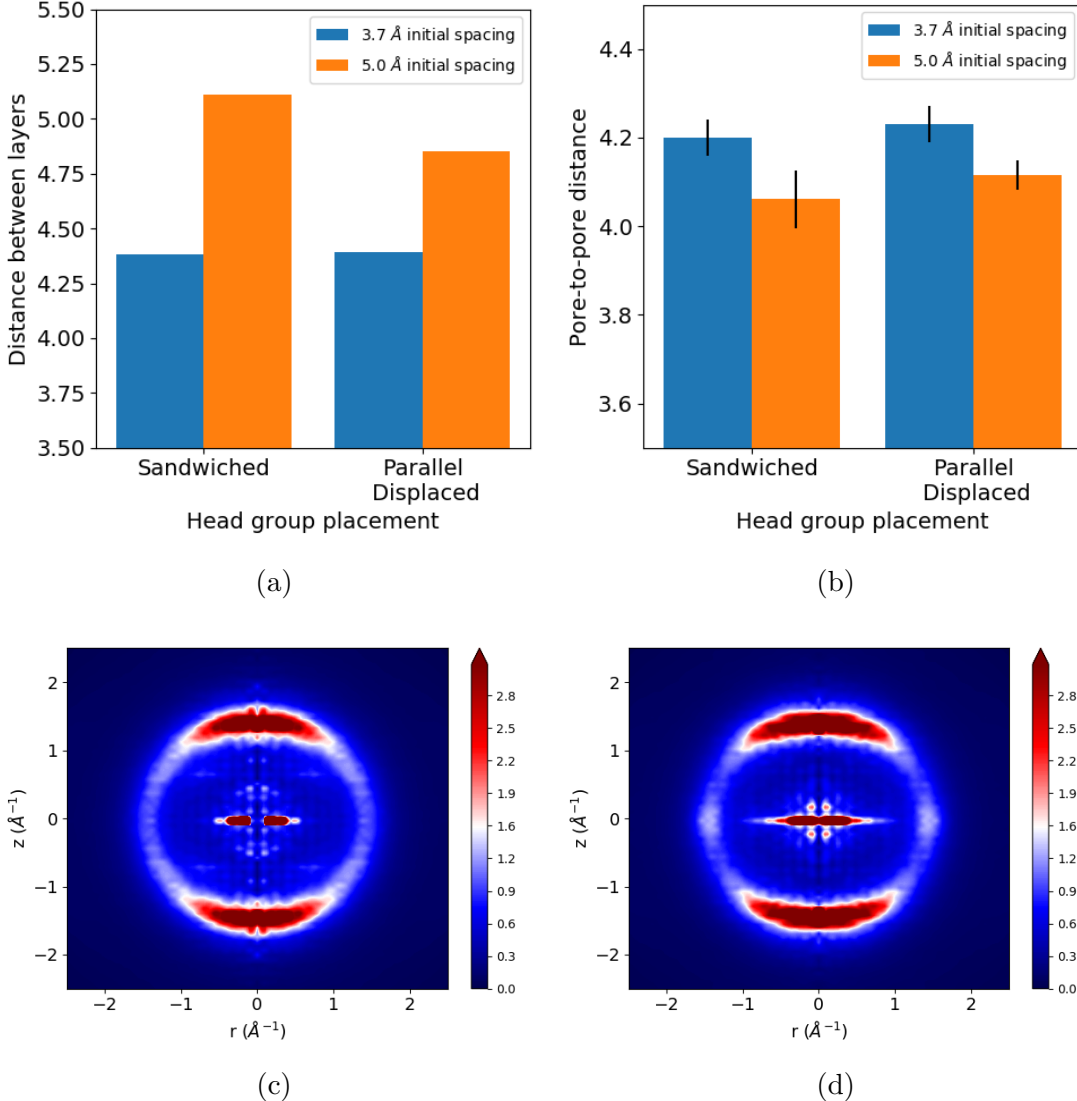


Figure 14: There are distinct differences between the disordered and ordered pore systems. When layers are initially stacked 5 Å apart, the distance between layers increases (a) and the pore spacing decreases (b) in comparison to the ordered pore systems. The simulated XRD patterns of disordered pore systems are also appreciably different, most notably in the region bounded by R-alkanes. The disordered pore systems started in the parallel displaced configuration (c) does not show R-spots or R- $\pi$  which suggests that head groups are not associating with each other and tails are distributed nearly isotropically. The disordered pore system started in the sandwiched configuration (d) does not show R- $\pi$  but R-spots are present in different locations because the tails are packed in a different motif.

more rotational freedom about the xy plane likely due to the larger separation between layers. Similarly, monomers situated in the sandwiched configuration are constrained by other

monomers stacked directly above and below them, while monomers in the parallel displaced configuration have no direct neighbors vertically which provides them with more rotational freedom.

**Table 1:** The nematic order parameter, S, is higher when layers are initially spaced 3.7 Å apart. In general, the sandwiched configuration has higher nematic order than the parallel displaced configuration. Correlation lengths are higher in the ordered pore basin. Correlation lengths in the disordered pore basin are in closer agreement with experiment. WHY IS THIS BOLD??!

System	Correlation Length (Å)	Nematic Order Parameter (S)
Sandwiched, Ordered	$41 \pm 3$	$0.659 \pm 0.003$
Parallel Displaced, Ordered	$86 \pm 14$	$0.601 \pm 0.003$
Sandwiched, Disordered	$17 \pm 3$	$0.565 \pm 0.002$
Parallel Displaced, Disordered	$9 \pm 1$	$0.503 \pm 0.002$
Experiment	$10 \pm 1$	—

We observe evidence of disorder in the xy plane of the disordered pore basin when we plot the two dimensional pair distribution function,  $g(x, y)$ , between the centers of mass of monomer phenyl rings (Figure 15). The difference is most apparent in the plots of the sandwiched configurations. In the ordered pore basin, head groups primarily stay stacked on top of each other while in the disordered pore basin, head groups exhibit more motion about the pore center and even drift into the middle of the pore.  $g(x, y)$  for the parallel displaced configuration is less informative since adjacent layers are displaced in a way that occupies the gaps that are seen in  $g(x, y)$  for the sandwiched configuration

## Slow dynamics

We observe unusually slow dynamics in our system. Typical diffusion constants for columnar liquid crystals have been reported to be on the order of  $10^{-11} \text{ m}^2/\text{s}$ .<sup>40</sup> We measured the diffusion constants of monomers in each of the systems we studied (Table 2) and learned that they are all on the order of  $10^{-14} \text{ m}^2/\text{s}$ . Our systems may be frozen in a glassy state. It is also possible that we are simply observing characteristics of the experimental system.

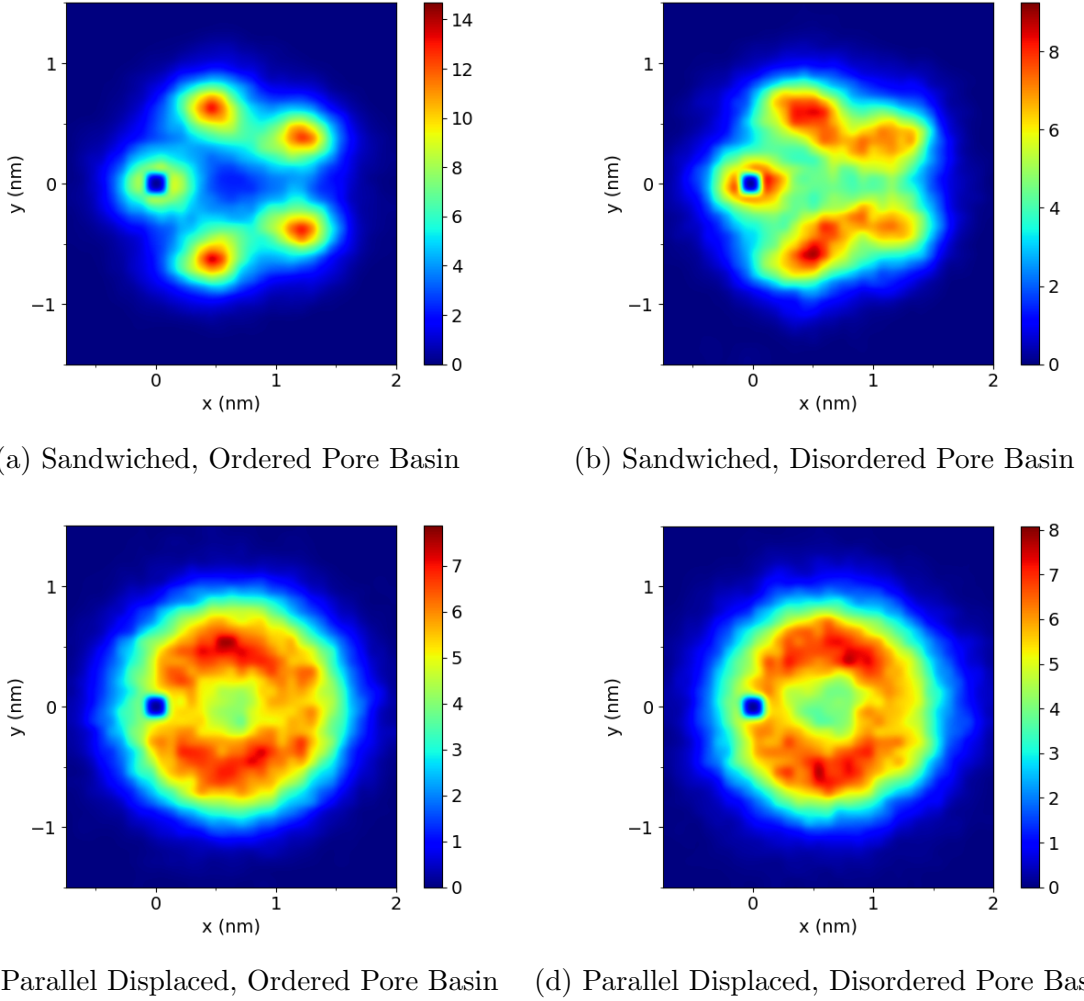


Figure 15:  $g(x,y)$  for sandwiched and parallel displaced configurations in the ordered and disordered pore basins illustrates the increase in xy plane disorder when initial configuration layer stacking distance is increase from 3.7 Å to 5 Å apart.

There has been no experimental work done to study diffusion of NA-GA3C11 monomers in the Col<sub>h</sub> system and no measurement of the glass transition temperature. Such a low diffusion constant is not unheard of. A more recent study reported a diffusion constant of  $1.2 \times 10^{-14} m^2/s$  for a different liquid crystal that formed a hexagonal columnar phase.<sup>41</sup>

It is possible that our equilibration procedure may induce glassy phase configurations. We have already shown that our system has some dependence on initial configuration. It is conceivable that after a fast initial relaxation, the system gets locked into a structure close to its initial configuration. The glassy state of these systems may be the reason we observe such high correlation lengths in the ordered pore basin systems. Unfortunately, we are unable to resolve the exact atomistic structure using existing experimental techniques, so we are left to find out which initial configuration results in a model with the closest match to experimental data.

**Table 2:** The diffusion constants for all systems are on the order of  $10^{-14} m^2/s$  which is three orders of magnitude lower than literature values.

System	Diffusion Constant ( $m^2/s$ )
Sandwiched, Ordered	$10^{-14}$
Parallel Displaced, Ordered	$10^{-14}$
Sandwiched, Disordered	$10^{-14}$
Parallel Displaced, Disordered	$10^{-14}$

### Chemical composition of pore columns

In order to address question (5), we plotted the number densities of heavy atoms in the head group, carbon atoms in the tail region and all sodium ions (Figure 16). For the head group region, we used the carbon atoms making up the aromatic ring. For the tail region we used only carbon atoms of the monomer tails (See Supporting Information for diagram). We average the histograms over at least 50 ns of equilibrated trajectory.

In all cases, the space in the pore region is filled with sodium ions and head groups. Systems in the ordered pore basin are less dense in the center of the pore. In both the

sandwiched and parallel displaced configurations, we see the density of head groups and sodium ions fall to less than 50% of its maximum at  $r = 0$  (Fig. 16b). The situation is most pronounced in the sandwiched configuration where the maximum head group density occurs 0.44 nm from the pore center. The parallel displaced configuration reaches its maximum 0.35 nm from the pore center. In contrast, both disordered pore systems show very little difference in density from its maximum. This implies a more uniform distribution of head groups within the pore center. This is the same conclusion drawn from the plots of  $g(x, y)$  (Figure 15).

There is a partition between the hydrophobic and hydrophilic regions, however it is a gradient in composition, rather than an abrupt division. The system does not confine sodium ions and head groups to just within the pore region. Assuming a pore radius of 0.6 nm, we see in all cases, that 19% of sodium ions exist outside the pore region (except sandwiched, ordered pore, where 16% are outside the pore). Additionally, we see that in all cases, about 3% of the plotted tail density is located within the pore region (except sandwiched, ordered pore, where 1.5% are within the pore region). These observations bring into question how one should define a pore in these types of systems. One usually measures a membrane's pore radius based on the size of a molecule it can reject, however it is not clear where the edges of the pores are and what size molecule would fit through. We leave these investigations for a future study.

## Effect of Water on Structure

We explored the affect of water on pore structure, addressing question (6), by preparing parallel displaced and sandwiched configurations according to the wet equilibration procedure. There is no experimental measurement of trace water concentration in the pores so we tested a range of water concentrations from 1 to 5 percent. Our lower bound models a system with on average 2 water molecules for each monomer layer. Figure 17 shows the simulated diffraction patterns resulting from each configuration.

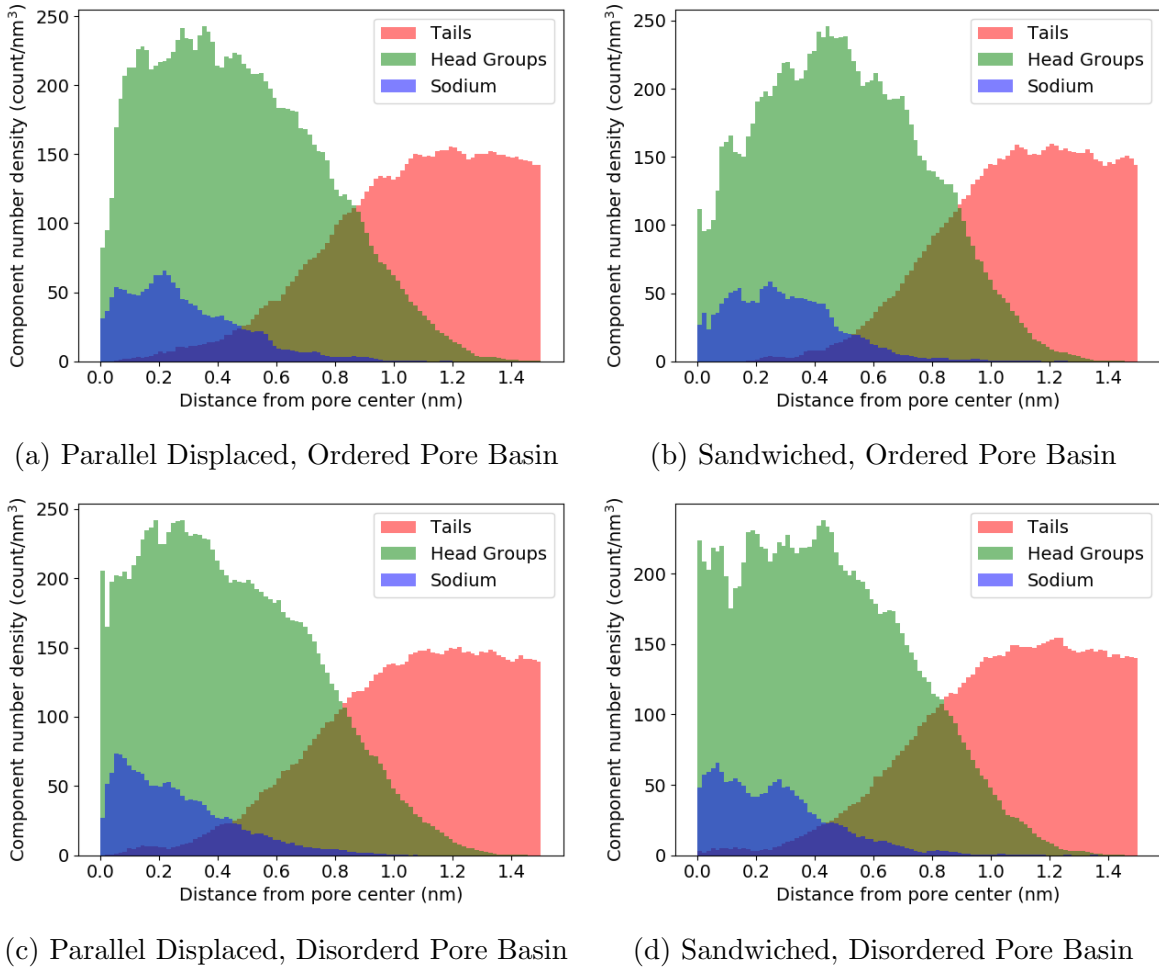


Figure 16: In all cases, the component radial distribution functions exhibit a composition gradient transitioning from the hydrophilic to the hydrophobic regions. Systems with layers initially spaced 3.7 Å apart in the parallel displaced (a), and sandwiched (b) configurations both show the highest concentrations of ions and head groups away from the pore center. Systems with layers initially spaced 5 Å apart (c) and (d), both show the highest concentrations of ions and head groups near the pore center, implying a more uniform, disordered pore.

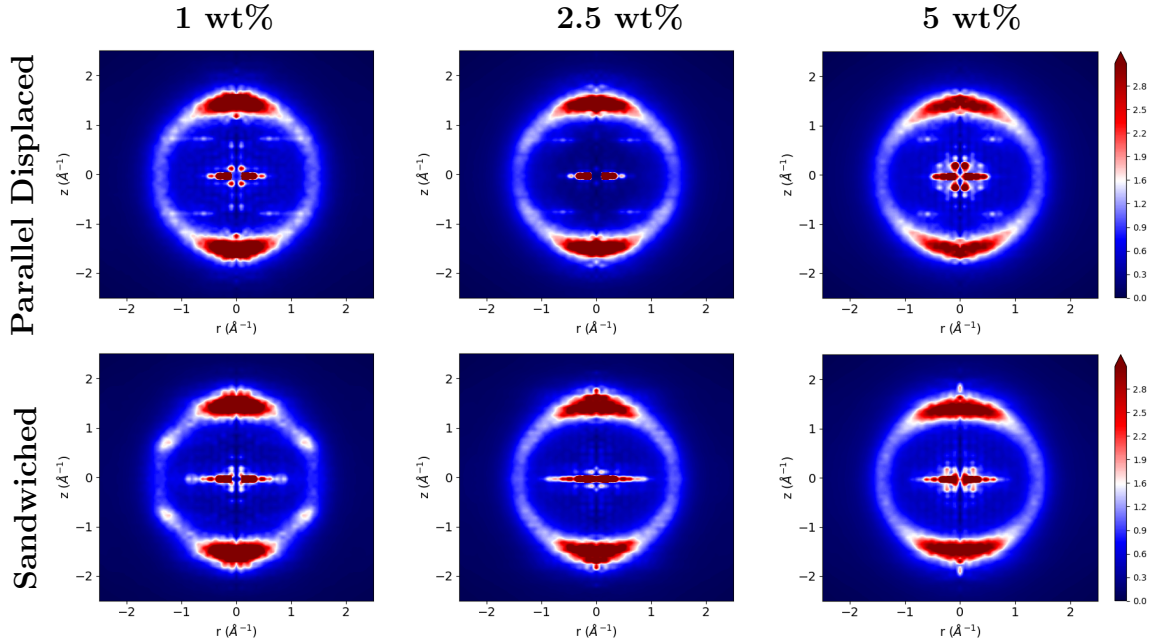


Figure 17: Simulated XRD patterns indicate that systems with added water are not as structured as the dry systems. As increasing amounts of water are added to both systems,  $R-\pi$  fades. When 2.5 wt% water is added to the sandwiched system,  $R-\pi$  gains back some intensity, but its magnitude is not greater than the dry system.  $R$ -spots also disappears as water is added. It is absent in all parallel displaced simulations, but fades gradually as water is added to the sandwiched configuration.

In all cases, water disrupts structuring of the model. When we add water to the system, the intensity of the reflections decrease. In systems built with 5 wt% water, R- $\pi$  and R-spots become nearly indistinguishable from R-alkanes.

In systems built with 5 wt% water, the pore region becomes filled with water. We plotted the number density of components in this system. As with the dry systems, we see a gradual compositional transition from hydrophilic to hydrophobic. We see that the pores become a mixture of water molecules and sodium ions (Fig. 18).

The membrane swells when we introduce water. The location of maximum head group density shifts from 0.35 to 0.62 nm and from 0.44 to 0.61 nm in the parallel displaced and sandwiched configurations respectively. Again, we observe the existence of ions, head groups and water outside the pore region, however in the hydrated system, the head groups drift beyond 1.5 nm from the pore center. In the dry systems, head groups did not wander beyond 1.4 nm from the pore center. Both observations suggest that water pushes all components radially outward from the pore center, characteristic of a swelling process. The plots of  $g(x, y)$  for dry and wet systems are compared in Figure 19. They further illustrate how the system swells in the presence of water. This system is a closer representation of the H<sub>II</sub> phase which is typically synthesized with ca. 8 wt% water. Further investigation of hydrated systems can help unravel the mechanisms for selective transport in separations of aqueous solutions.

Water is not necessary to maintain an ordered pore structure. We do not eliminate the possibility that water is necessary in order to drive self-assembly, but studying the mechanisms of self-assembly is beyond the scope of this work. According to our model, once the system has formed the Col<sub>h</sub> phase, adding water only drives disorder of the pore structure. In the true equilibrium configuration, if water exists, it is primarily confined to the pore region where there is no driving force for aggregation of water molecules. In the case of trace water, water molecules will be too sparse to form a hydrogen bonding network.

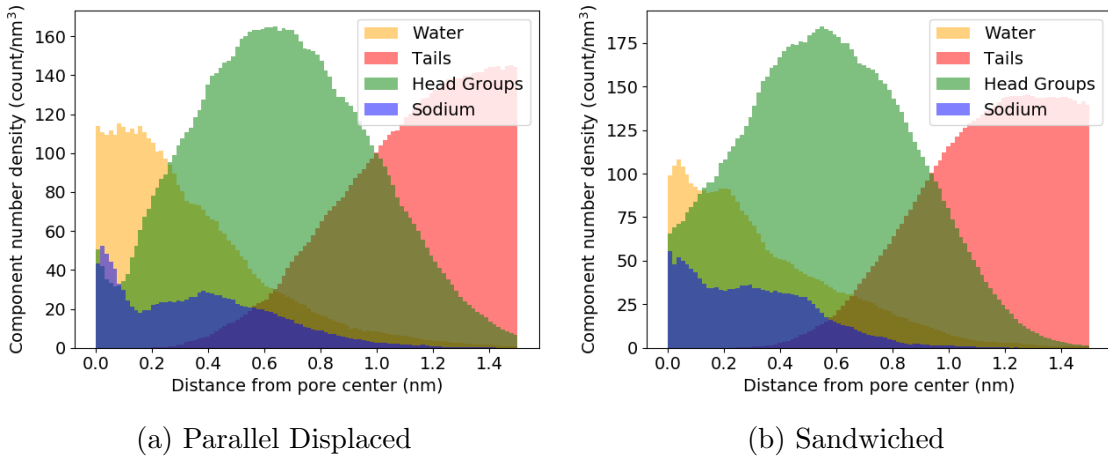


Figure 18: Water fills the membrane pores in the parallel displaced (a) and sandwiched (b) configurations. Head groups in the sandwiched configuration sit closer to the pore center than they do in the parallel displaced configuration. Both systems are composed primarily of water close to the pore center.

## Model Ionic Conductivity Measurements

We used the equilibrated parallel displaced system in the ordered pore basin to calculate ionic conductivity since its structure is the closest match to experiment. The model gives reasonable estimates of ionic conductivity when compared to experiment. We compare calculated values of ionic conductivity obtained using the Nernst-Einstein relation and Collective Diffusion model in Figure 20. The two methods agree with each other within error, although the uncertainty obtained using the Collective Diffusion model is much higher. We require much longer simulations to lower the uncertainty, however it is not feasible to do so with a large system. We will only use the Nernst-Einstein relation in future calculations of this type.

The calculated values of ionic conductivity are higher than experiment by an order of magnitude. One can justify the reason for this result by considering the real system studied experimentally. The ionic conductivity measurement to which we are comparing was done with a  $80\text{ }\mu\text{m}$  thick film, nearly 10,000 times thicker than our simulated system. The thick film is likely imperfectly aligned and has defects leading to non-contiguous pores. It has been shown that there is a large dependence of ionic conductivity on the alignment of the

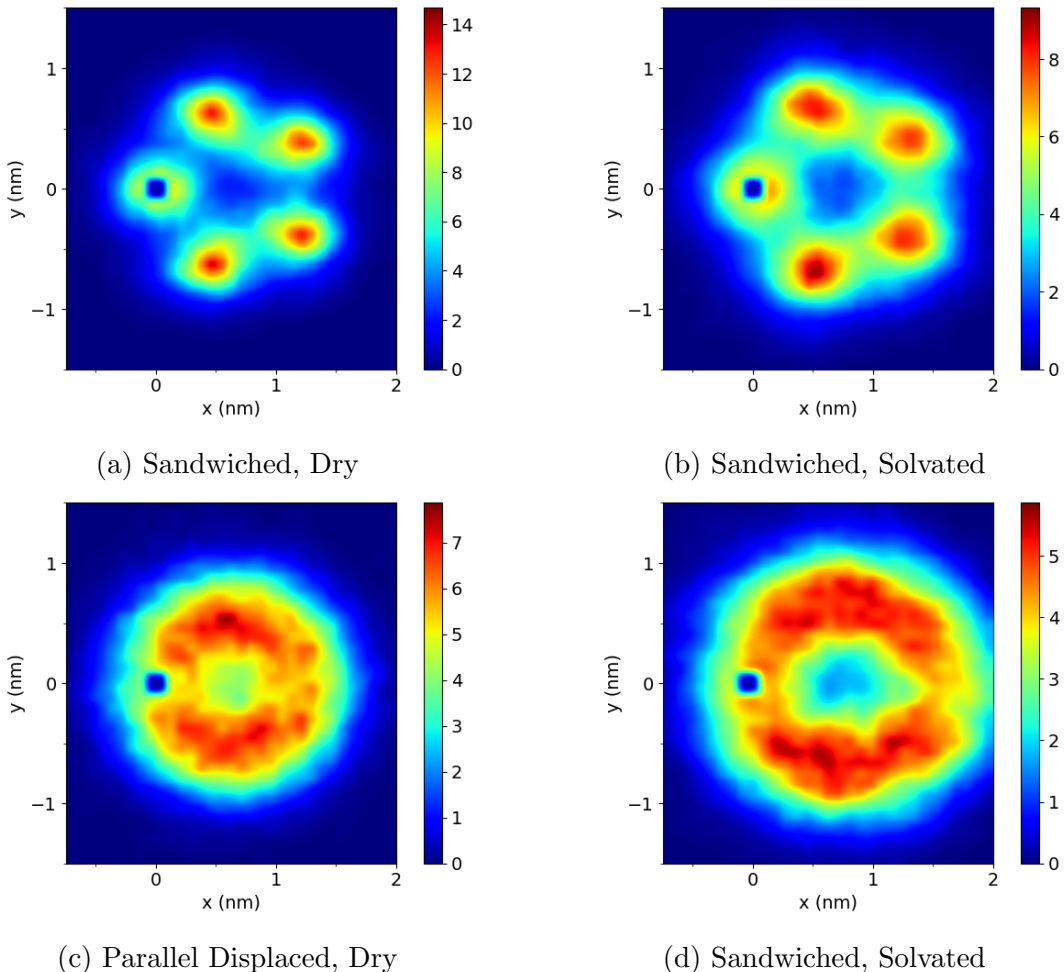


Figure 19:  $g(x, y)$  of monomer head groups illustrates how the pores swell in the presence of water.

pores. The ionic conductivity of an isotropically aligned film is ca. 85 times lower than that of a nearly aligned film referenced here.<sup>11</sup> We hypothesize that a thin, perfectly aligned film would have a value of ionic conductivity in closer agreement with our model.

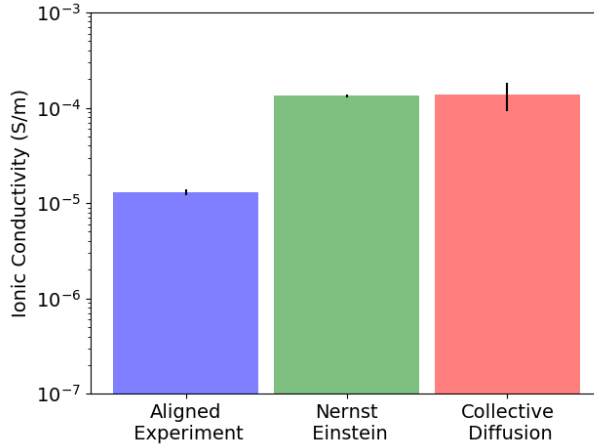


Figure 20: The collective diffusion model and the nernst-einstein relation yield agreeing values of ionic conductivity. Both methods give calculated values of ionic conductivity an order of magnitude higher than the experimental value.

## Effect of Crosslinking

The system's structure and physical characteristics did not change significantly when we applied the cross-linking algorithm to the equilibrated parallel-displaced configuration in the ordered pore basin. We simulated the cross-linked system in the NPT ensemble for 100 ns. After the system is cross-linked, the distance between pores shrinks by 0.4 Å and the distance between layers increases by 0.04 Å. All major features are still present in the simulated XRD patterns, however at lower intensities (Fig. 21a). We calculated the ionic conductivity using the Nernst-Einstein relation and found that it is lower in the cross-linked system (Fig. 21b).

## Conclusion

We have used a detailed molecular model of the Col<sub>h</sub> phase formed by Na-GA3C11 in order to study its nanoscopic structure. While there have been efforts to model formation of

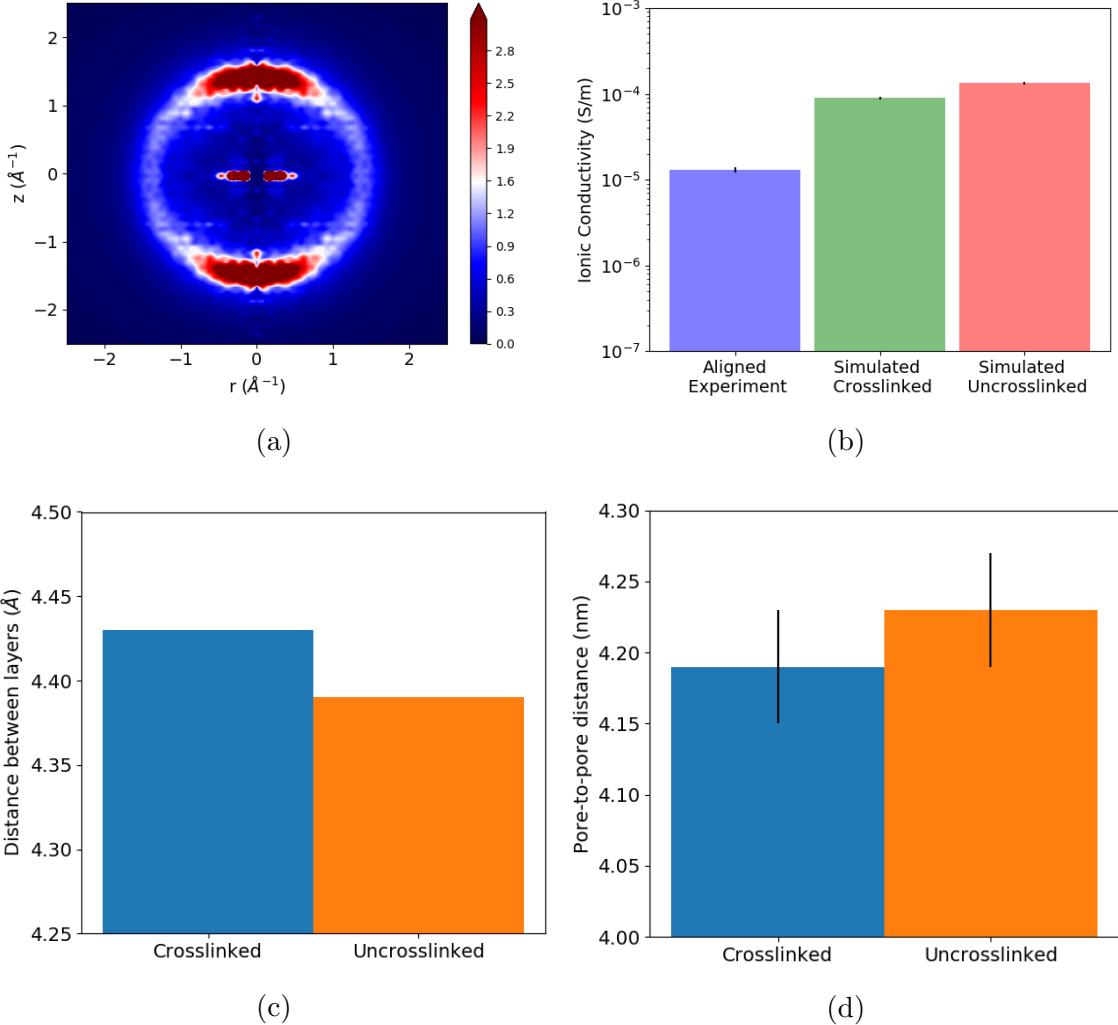


Figure 21: Applying our simulated crosslinking mechanism to an equilibrium configuration causes slight changes to the system's physical and structural properties. (a) Reflections produced by the cross-linked configuration are faded relative to the uncross-linked system. (b) The ionic conductivity is smaller relative to the uncross-linked system, but still much larger than the experimental value. When the system is cross-linked, the distance between layers increases (c) and the pore spacing decreases (d)

various liquid crystalline phases with molecular dynamics, to our knowledge there have been no studies which attempt to examine their structure with the same level of detail presented here.

Evidence strongly supports that monomers stay partitioned into layers which stack to create pores and that each layer contains 5 monomers. We see periodic spacing of layers based on the z-direction correlation function,  $g(z)$ , of atoms in the tails and separately of atoms in the head groups. Systems not built with 5 monomers per layer result in assemblies whose pore-to-pore spacing is inconsistent with experiment.

We have explored the affect of two different  $\pi$ - $\pi$  stacking modes on the equilibrated membrane structure. Simulated diffraction patterns generated from MD trajectories suggest that the parallel-displaced configuration produces a structure with the closest match to experiment.

We have observed a number of metastable configurations. We witnessed long-term stability of systems built with a varied number of monomers per layer as well as in different  $\pi$ - $\pi$  stacking configurations. We also examined how the structure changes based on the initial distance between layers and showed how systems differ when built with layers spaced 5 Å versus 3.7 Å apart. The configuration that showed the greatest agreement with experiment was built in the parallel-displaced configuration, with 5 monomers per layer and an initial layer spacing of 3.7 Å.

We characterized the environment centered around the membrane pores and learned that the pores are generally filled by monomer head groups and sodium ions. Membranes prepared in the sandwiched configuration have lower density pores. We also observed that there is not a hard partition between hydrophobic and hydrophilic regions, rather there is a gradient. This finding has raised questions about the nature of any size-exclusion separations.

We learned that we do not need water to create well-defined pore structures. Systems whose pores were filled with varying amounts of water showed a decrease in structuring relative to dry systems.

We justified that our system can reasonably estimate ionic conductivity. Our calculations are about 1 order of magnitude higher than experiment, however that is to be expected since we are simulating a perfectly straight and defect-free membrane.

Finally, we verified that our conclusions do not change when the system is cross-linked by the algorithm we implemented. The diffraction pattern weakens relative to the uncross-linked system, the ionic conductivity drops by a factor of ca. 1.5, in closer agreement with experiment, the pore spacing decreases and the membrane becomes thicker.

We acknowledge that our simulated system exhibits glassy dynamics. The measured diffusion constants of monomers are three orders of magnitude lower than expected. It is possible that our equilibration procedure induces these types of metastable phases. It is also possible that the observed dynamics are characteristic of the real system. We took great care to overcome the potential limitations of our equilibration procedure and have come up with a structure that is in good agreement with experimental data.

With the structural understanding gained by these simulations, we will evaluate transport of various solutes within the system. We will apply the knowledge gained from this study in order to suggest improvements to the existing system as well as to evaluate new unsynthesized LLC systems.

## References

- (1) Dischinger, S. M.; Rosenblum, J.; Noble, R. D.; Gin, D. L.; Linden, K. G. Application of a lyotropic liquid crystal nanofiltration membrane for hydraulic fracturing flowback water: Selectivity and implications for treatment. *Journal of Membrane Science* **2017**, *543*, 319–327.
- (2) Theodori, G. L.; Luloff, A.; Willits, F. K.; Burnett, D. B. Hydraulic fracturing and the management, disposal, and reuse of frac flowback waters: Views from the public in the Marcellus Shale. *Energy Research & Social Science* **2014**, *2*, 66–74.
- (3) Gin, D. L.; Bara, J. E.; Noble, R. D.; Elliot, B. J. Polymerized Lyotropic Liquid Crystal Assemblies for Membrane Applications. *Macromolecular Rapid Communications* **2008**, *29*, 367–389.
- (4) Wijmans, J. G.; Baker, R. W. The solution-diffusion model: a review. *Journal of Membrane Science* **1995**, *107*, 1–21.
- (5) Smith, R. C.; Fischer, W. M.; Gin, D. L. Ordered Poly(p-phenylenevinylene) Matrix Nanocomposites via Lyotropic Liquid-Crystalline Monomers. *Journal of the American Chemical Society* **1997**, *119*, 4092–4093.
- (6) Zhou, M.; Kidd, T. J.; Noble, R. D.; Gin, D. L. Supported Lyotropic Liquid-Crystal Polymer Membranes: Promising Materials for Molecular-Size-Selective Aqueous Nanofiltration. *Adv. Mater.* **2005**, *17*, 1850–1853.
- (7) Donnan, F. G. Theory of membrane equilibria and membrane potentials in the presence of non-dialysing electrolytes. A contribution to physical-chemical physiology. *Journal of Membrane Science* **1995**, *100*, 45–55.
- (8) Hatakeyama, E. S.; Gabriel, C. J.; Wiesnauer, B. R.; Lohr, J. L.; Zhou, M.; Noble, R. D.; Gin, D. L. Water filtration performance of a lyotropic liquid crystal polymer

- membrane with uniform, sub-1-nm pores. *Journal of Membrane Science* **2011**, *366*, 62–72.
- (9) Hatakeyama, E. S.; Wiesnauer, B. R.; Gabriel, C. J.; Noble, R. D.; Gin, D. L. Nanoporous, Bicontinuous Cubic Lyotropic Liquid Crystal Networks via Polymerizable Gemini Ammonium Surfactants. *Chem. Mater.* **2010**, *22*, 4525–4527.
- (10) Carter, B. M.; Wiesnauer, B. R.; Hatakeyama, E. S.; Barton, J. L.; Noble, R. D.; Gin, D. L. Glycerol-Based Bicontinuous Cubic Lyotropic Liquid Crystal Monomer System for the Fabrication of Thin-Film Membranes with Uniform Nanopores. *Chem. Mater.* **2012**, *24*, 4005–4007.
- (11) Feng, X.; Tousley, M. E.; Cowan, M. G.; Wiesnauer, B. R.; Nejati, S.; Choo, Y.; Noble, R. D.; Elimelech, M.; Gin, D. L.; Osuji, C. O. Scalable Fabrication of Polymer Membranes with Vertically Aligned 1 nm Pores by Magnetic Field Directed Self-Assembly. *ACS Nano* **2014**, *8*, 11977–11986.
- (12) Matyka, M.; Khalili, A.; Koza, Z. Tortuosity-porosity relation in porous media flow. *Phys. Rev. E* **2008**, *78*, 026306.
- (13) Feng, X.; Nejati, S.; Cowan, M. G.; Tousley, M. E.; Wiesnauer, B. R.; Noble, R. D.; Elimelech, M.; Gin, D. L.; Osuji, C. O. Thin Polymer Films with Continuous Vertically Aligned 1 nm Pores Fabricated by Soft Confinement. *ACS Nano* **2016**, *10*, 150–158.
- (14) Resel, R.; Leising, G.; Markart, P.; Kriechbaum, M.; Smith, R.; Gin, D. Structural properties of polymerised lyotropic liquid crystals phases of 3,4,5-tris(\$mega\$-acryloxyalkoxy)benzoate salts. *Macromolecular Chemistry and Physics* **2000**, *201*, 1128–1133.
- (15) Zhu, X.; Scherbina, M.; Bakirov, A.; Gorzolnik, B.; Chvalun, S.; Beginn, U.; Moller, M. Methacrylated Self-Organizing 2,3,4-Tris(alkoxy)benzenesulfonate: A New Concept Toward Ion-Selective Membranes. *Chem. Mater.* **2006**, *18*, 4667–4673.

- (16) Gazit, E. A possible role for -stacking in the self-assembly of amyloid fibrils. *FASEB J* **2002**, *16*, 77–83.
- (17) Sinnokrot, M. O.; Valeev, E. F.; Sherrill, C. D. Estimates of the Ab Initio Limit for Interactions: The Benzene Dimer. *J. Am. Chem. Soc.* **2002**, *124*, 10887–10893.
- (18) Waller, M. P.; Robertazzi, A.; Platts, J. A.; Hibbs, D. E.; Williams, P. A. Hybrid density functional theory for -stacking interactions: Application to benzenes, pyridines, and DNA bases. *J. Comput. Chem.* **2006**, *27*, 491–504.
- (19) Ringer, A. L.; Sinnokrot, M. O.; Lively, R. P.; Sherrill, C. D. The Effect of Multiple Substituents on Sandwich and T-Shaped Interactions. *Chem. Eur. J.* **2006**, *12*, 3821–3828.
- (20) McIntosh, T. J.; Simon, S. A.; MacDonald, R. C. The organization of n-alkanes in lipid bilayers. *Biochimica et Biophysica Acta (BBA) - Biomembranes* **1980**, *597*, 445–463.
- (21) Govind, A. S.; Madhusudana, N. V. A simple molecular theory of smectic-C liquid crystals. *EPL* **2001**, *55*, 505.
- (22) Wang, J.; Wolf, R. M.; Caldwell, J. W.; Kollman, P. A.; Case, D. A. Development and testing of a general amber force field. *J. Comput. Chem.* **2004**, *25*, 1157–1174.
- (23) Wang, J.; Wang, W.; Kollman, P. A.; Case, D. A. Automatic atom type and bond type perception in molecular mechanical calculations. *Journal of Molecular Graphics and Modelling* **2006**, *25*, 247–260.
- (24) Case, D.; Betz, R.; Botello-Smith, W.; Cerutti, D.; Cheatham, T., III; Darden, T.; Duke, R.; Giese, T.; Gohlke, H.; Goetz, A. et al. AmberTools16. 2016.
- (25) Bekker, H.; Berendsen, H. J. C.; Dijkstra, E. J.; Achterop, S.; van Drunen, R.; van der Spoel, D.; Sijbers, A.; Keegstra, H.; Reitsma, B.; Renardus, M. K. R. Gromacs: A parallel computer for molecular dynamics simulations. *Physics Computing* **1993**,

- (26) Berendsen, H. J. C.; van der Spoel, D.; van Drunen, R. GROMACS: A message-passing parallel molecular dynamics implementation. *Computer Physics Communications* **1995**, *91*, 43–56.
- (27) Van Der Spoel, D.; Lindahl, E.; Hess, B.; Groenhof, G.; Mark, A. E.; Berendsen, H. J. C. GROMACS: Fast, flexible, and free. *J. Comput. Chem.* **2005**, *26*, 1701–1718.
- (28) Hess, B.; Kutzner, C.; van der Spoel, D.; Lindahl, E. GROMACS 4: Algorithms for Highly Efficient, Load-Balanced, and Scalable Molecular Simulation. *J. Chem. Theory Comput.* **2008**, *4*, 435–447.
- (29) Mondal, J.; Mahanthappa, M.; Yethiraj, A. Self-Assembly of Gemini Surfactants: A Computer Simulation Study. *J. Phys. Chem. B* **2013**, *117*, 4254–4262.
- (30) Martnez, L.; Andrade, R.; Birgin, E. G.; Martnez, J. M. PACKMOL: A package for building initial configurations for molecular dynamics simulations. *J. Comput. Chem.* **2009**, *30*, 2157–2164.
- (31) Young, R.; Lovell, P. *Introduction to Polymers*, 3rd ed.; CRC Press, 2011.
- (32) Chodera, J. D. A Simple Method for Automated Equilibration Detection in Molecular Simulations. *Journal of Chemical Theory and Computation* **2016**, *12*, 1799–1805.
- (33) Shirts, M. R.; Chodera, J. D. Statistically optimal analysis of samples from multiple equilibrium states. *The Journal of Chemical Physics* **2008**, *129*, 124105.
- (34) Kuriabova, T.; Betterton, M. D.; Glaser, M. A. Linear aggregation and liquid-crystalline order: comparison of Monte Carlo simulation and analytic theory. *J. Mater. Chem.* **2010**, *20*, 10366–10383.
- (35) Einstein, A. Investigations on the theory of the brownian movement. *Dover Publications* **1956**,

- (36) Liu, Y.; Zhu, F. Collective diffusion model for ion conduction through microscopic channels. *Biophys. J.* **2013**, *104*, 368–376.
- (37) Baker, C. M. Polarizable force fields for molecular dynamics simulations of biomolecules. *WIREs Comput Mol Sci* **2015**, *5*, 241–254.
- (38) Chaikin, P.; Lubensky, T. *Principles of condensed matter physics*, 1st ed.; Cambridge University Press, 1995.
- (39) Small, D. M. Lateral chain packing in lipids and membranes. *J. Lipid Res.* **1984**, *25*, 1490–1500.
- (40) Dong, R. Y.; Goldfarb, D.; Moseley, M. E.; Luz, Z.; Zimmermann, H. Translational diffusion in discotic mesophases studied by the nuclear magnetic resonance pulsed field gradient method. *J. Phys. Chem.* **1984**, *88*, 3148–3152.
- (41) Dvinskikh, S. V.; Fur, I.; Zimmermann, H.; Maliniak, A. Molecular self-diffusion in a columnar liquid crystalline phase determined by deuterium NMR. *Phys. Rev. E* **2002**, *65*, 050702.

## Graphical TOC Entry

